HHS Public Access

Author manuscript

Cell Rep. Author manuscript; available in PMC 2021 November 26.

Published in final edited form as:

Cell Rep. 2021 November 16; 37(7): 110008. doi:10.1016/j.celrep.2021.110008.

Sterols lower energetic barriers of membrane bending and fission necessary for efficient clathrin-mediated endocytosis

Ruthellen H. Anderson[1,2], **Kem A. Sochacki**[3], **Harika Vuppula**[4,5], **Brandon L. Scott**[6], **Elizabeth M. Bailey**[4,5], **Maycie M. Schultz**[2], **Jason G. Kerkvliet**[4,5], **Justin W. Taraska**[3], **Adam D. Hoppe**[4,5,*], **Kevin R. Francis**[2,7,8,*]

[1]Sanford School of Medicine, University of South Dakota, Sioux Falls, SD 57105, USA

[2]Cellular Therapies and Stem Cell Biology Group, Sanford Research, Sioux Falls, SD 57104, USA

[3]Laboratory of Molecular Biophysics, National Heart Lung and Blood Institute, National Institutes of Health, Bethesda, MD 20814, USA

[4]Department of Chemistry and Biochemistry, South Dakota State University, Brookings, SD 57007, USA

[5]BioSystems Networks and Translational Research Center, Brookings, SD 57007, USA

[6]Nanoscience and Nanoengineering, South Dakota School of Mines & Technology, Rapid City, SD 57701, USA

[7]Department of Pediatrics, Sanford School of Medicine, University of South Dakota, Sioux Falls, SD 57105, USA

[8]Lead contact

SUMMARY

Clathrin-mediated endocytosis (CME) is critical for cellular signal transduction, receptor recycling, and membrane homeostasis in mammalian cells. Acute depletion of cholesterol disrupts CME, motivating analysis of CME dynamics in the context of human disorders of cholesterol metabolism. We report that inhibition of post-squalene cholesterol biosynthesis impairs CME. Imaging of membrane bending dynamics and the CME pit ultrastructure reveals prolonged clathrin pit lifetimes and shallow clathrin-coated structures, suggesting progressive impairment of curvature generation correlates with diminishing sterol abundance. Sterol structural requirements for efficient CME include 3′ polar head group and B-ring conformation, resembling

*Correspondence: adam.hoppe@sdstate.edu (A.D.H.), kevin.francis@sanfordhealth.org (K.R.F.).

AUTHOR CONTRIBUTIONS

Conceptualization, R.H.A. and K.R.F.; methodology, R.H.A., K.R.F., A.D.H., B.L.S., and J.G.K.; investigation, R.H.A., M.M.S., K.A.S., B.L.S., and E.M.B.; software, H.V. and B.L.S.; writing—original draft, R.H.A.; writing—review & editing, R.H.A., K.R.F., A.D.H., B.L.S., E.M.B., K.A.S., and J.W.T.; funding acquisition, R.H.A. and K.R.F.; supervision, K.R.F., A.D.H., and J.W.T.

SUPPLEMENTAL INFORMATION

Supplemental information can be found online at https://doi.org/10.1016/j.celrep.2021.110008.

DECLARATION OF INTERESTS

The authors declare no competing or financial interests.

the sterol structural prerequisites for tight lipid packing and polarity. Furthermore, Smith-Lemli-Opitz fibroblasts with low cholesterol abundance exhibit deficits in CME-mediated transferrin internalization. We conclude that sterols lower the energetic costs of membrane bending during pit formation and vesicular scission during CME and suggest that reduced CME activity may contribute to cellular phenotypes observed within disorders of cholesterol metabolism.

Graphical Abstract

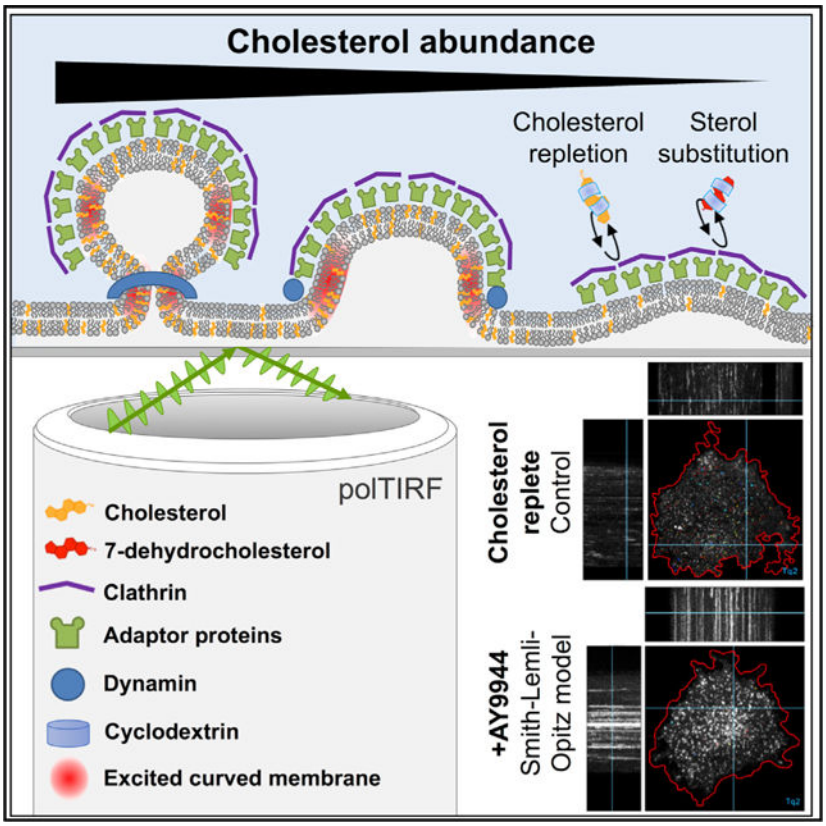

In brief

Anderson et al. demonstrate that sterol abundance and identity play a dominant role in facilitating clathrin-mediated endocytosis. Detailed analyses of clathrin-coated pits under sterol depletion support a requirement for sterol-mediated membrane bending during multiple stages of endocytosis, implicating endocytic dysfunction within the pathogenesis of disorders of cholesterol metabolism.

INTRODUCTION

Lipid composition is critical to the biophysical properties of membrane bilayers, permitting the maintenance of essential cellular functions such as membrane trafficking and signal transduction (Kusumi et al., 2012). Cholesterol is recognized as a major regulator of lipid organization as its unique structure influences lipid packing, protein interactions, and global membrane properties (Maxfield and Tabas, 2005). Synthesized *de novo* in the endoplasmic

reticulum or derived from circulating low-density lipoproteins, unesterified cholesterol is distributed heterogeneously among various cell membranes, being predominately enriched at the plasma membrane (PM) where it accounts for up to 45% of the total lipids present (Das et al., 2013) and 60%–90% of total cellular cholesterol (de Duve 1971; Lange et al., 1989). The importance of cholesterol composition to PM structure and function is reflected in the tight regulation of intracellular transport and highly coordinated synthetic and efflux mechanisms maintaining physiologic cholesterol levels (Luo et al., 2019; Nohturfft et al., 1998; Sun et al., 2005; Vedhachalam et al., 2007).

Membrane properties, including rigidity and tension, are especially pertinent to highly dynamic membrane remodeling processes such as endocytosis (Hassinger et al., 2017). As the major pathway regulating receptor-mediated signaling, clathrin-mediated endocytosis (CME) mediates nutrient uptake, signal transduction, receptor recycling and desensitization, and developmental regulation (Kaksonen and Roux, 2018). Evidence for cholesterol's role in CME has been demonstrated by acute stripping of membrane cholesterol by using methyl-beta-cyclodextrin (MβCD) (Rodal et al., 1999; Subtil et al., 1999). Although MβCD is a relatively non-specific cholesterol extraction method contingent upon the carrier's hydrophobic cavity, these classic experiments suggest a strong defect in clathrin-coated pit budding and internalization upon MβCD treatment.

Amid the extensive CME machinery described to date, the influence of cholesterol on PM architecture may be overlooked as an active component within assembly, curvature generation, and scission of clathrin-coated pits. CME is initiated by the recruitment of clathrin triskelia by adaptor and accessory proteins to sites of phosphatidylinositol-4,5-bisphosphate (PtdIns(4,5)P_2)-enriched PM (Cocucci et al., 2012). This assembly process may be sensitive to alterations of lipid packing or shielding of charges secondary to cholesterol availability (Hirama et al., 2017). Progression of the PM from flat to highly curved clathrin-coated vesicles also requires overcoming membrane stiffness and tension generated by lateral membrane recruitment and opposed by membrane-cytoskeletal adhesions (Bucher et al., 2018; Scott et al., 2018). Recruitment of epsin NH2-terminal homology (ENTH), AP180 N-terminal homology (ANTH), and later Bin/Amphiphysin/Rvs (BAR)-domain-containing proteins likely contribute to the energy required for membrane bending (Liu et al., 2009; McMahon and Gallop, 2005; Miller et al., 2015). By interacting with these curvature effectors and stabilizing positive PM fluctuations, the clathrin lattice is thought to act as a Brownian ratchet promoting curvature formation (Liu et al., 2009). This remodeling process creates energetically unfavorable membrane stress that may be alleviated by cholesterol through rapid transbilayer redistribution (Bruckner et al., 2009). During vesicular scission, an energetically costly constriction requiring steep membrane curvature must be achieved. The GTPase dynamin catalyzes this event by polymerizing into a helical coat and constricting the endocytic pit neck by guanosine triphosphate (GTP) hydrolysis and removal of dynamin subunits. However, previous work has demonstrated constriction alone is insufficient for scission to occur (Danino et al., 2004; Roux et al., 2006). Considering the severity of membrane bending at these sites, the mechanical properties of the PM immediately adjacent to the dynamin coat, including membrane tension and bending rigidity, are thought to influence scission (Morlot et al., 2012). Bursts of actin polymerization also help overcome resistance to membrane bending by providing additional force, leading to

vesicle internalization and scission (Collins et al., 2011; Grassart et al., 2014), especially in areas of high membrane tension (Boulant et al., 2011).

Cholesterol is a unique membrane lipid with competing influences on membrane mechanics. As described by the Helfrich bending Hamiltonian model (Helfrich, 1973), the curvature properties of a bilayer include bending rigidity and spontaneous curvature that reflect the effective "stiffness" of the membrane and account for the asymmetry of the leaflet constituents. Cholesterol and select sterols have the capacity to partition bilayers into liquid-ordered (L_o) or liquid-disordered (L_d) phases due to preferential tight packing as dependent upon the specific lipid architecture. Given this propensity to facilitate increased packing density and bilayer thickness, the addition of cholesterol can be expected to increase rigidity and impair deformation (Chakraborty et al., 2020; Henriksen et al., 2004). Paradoxically, numerous experiments indicate that removal of cholesterol from the PM does not soften the cell, possibly due to sub-membrane cortical actin (Ayee and Levitan, 2016). During spontaneous curvature, cholesterol behaves as an extremely negative curvature lipid in disordered membranes (Chen and Rand, 1997) but appears to have a net positive effect in the presence of saturated lipids. This information implies that cholesterol's spontaneous curvature may be strongly modulated by phase separation, acting to dynamically lower the bending modulus (Leibler, 1986; Sodt et al., 2016). Both lateral diffusion and the rapid transbilayer flip-flop of cholesterol may also relieve stress associated with membrane remodeling by alleviating the molecular disparities between the inner and outer PM leaflets (Bruckner et al., 2009; Lange et al., 1981). In contrast to other PM lipid components, cholesterol transbilayer flip-flop occurs within milliseconds (Choubey et al., 2013; Hamilton, 2003; Steck et al., 2002), a sufficient timescale to support local membrane remodeling during an endocytic event (Taylor et al., 2011). Additionally, phase separation is postulated to underlie membrane shape transitions by minimizing line tension between L_o and L_d domain boundaries, driving progressive curvature generation to neck structures (Jülicher and Lipowsky, 1993, 1996), and is implicated in the curvature and budding of artificial membranes (Bacia et al., 2005). This behavior has recently been reviewed as a driving force in other clathrin-independent endocytic pathways (Hilgemann et al., 2020) and during CME (Frey and Schwarz, 2020).

Human diseases associated with the disruption of cholesterol homeostasis may provide insight into the lipid-specific requirements of CME and find application of cellular trafficking within these disease states. Of these diseases, the best characterized one is Smith-Lemli-Opitz syndrome (SLOS) that is caused by genetic mutations within the post-squalene cholesterol synthesis enzyme 3β-hydroxy-steroid-ρ^7-reductase (DHCR7) (Wassif et al., 1998) and presents clinically with multiple congenital malformations and CNS dysfunction (Smith et al., 1964). Although clinical severity generally correlates inversely with residual enzymatic activity, significant phenotypic variability exists among similar pathogenic variants (Cunniff et al., 1997; Wassif et al., 2005; Waterham and Hennekam, 2012), ranging from mild cognitive impairment to embryonic lethality (Tint et al., 1995). The relative contribution of cholesterol depletion and/or accumulation of sterol precursors such as 7-dehydrocholesterol (7DHC) to disease pathogenesis also remains an open question (Wassif et al., 2017). To date, membrane defects within SLOS have primarily been attributed to the disruption of lipid rafts (Gou-Fàbregas et al., 2016; Keller et al., 2004). Nevertheless,

global effects on PM architecture may perturb lipid raft independent processes (Kwik et al., 2003; Sengupta et al., 2007; van Rheenen et al., 2005). One hypothesis suggests that SLOS pathogenesis manifests in a highly temporal and tissue-specific context, driven by changes in signal transduction (Tulenko et al., 2006). Thus, defining the effects of disrupted sterol synthesis on the major pathway regulating receptor-mediated signaling may provide insight into the molecular and cellular basis for the physiologic manifestations within these diseases.

In this study, we demonstrate that multiple stages of membrane remodeling during CME progression are sensitive to sterol-dependent membrane properties. The clathrin pit ultrastructure with cholesterol depletion exhibited asymmetric distorted structures consistent with aberrant membrane-bending trajectories, suggesting that clathrin lattice assembly competes with the elevated free energy costs of bending. To gain insight into the biophysical mechanisms facilitating membrane remodeling, we used cyclodextrin (CD)-mediated sterol substitution strategies to demonstrate that a small, C3 polar headgroup and B-ring conformation constitute structural requirements for supporting efficient CME. Finally, we present evidence for the disruption of CME dynamics within SLOS and conclude that sterol abundance lowers the energetic barrier for curvature generation during the initiation of membrane bending and formation of the vesicle neck during CME.

RESULTS

CME is inhibited by altered cholesterol homeostasis

To test the hypothesis that sterol homeostasis contributes to efficient CME, we evaluated CME during acute cholesterol depletion and perturbations of cholesterol synthesis in HEK293T cells. Endogenous cholesterol biosynthesis was induced by culturing cells in media containing 7.5% lipoprotein-deficient fetal bovine serum (LPDS). We used multiple targeting strategies to delineate the effects of cholesterol depletion versus terminal cholesterol precursor accumulation within the competing Bloch and Kandutsch-Russell (KR) pathways (Figure 1A). AY9944 dihydrochloride, a DHCR7 (Δ7-sterol reductase) inhibitor (Rahier and Taton, 1996), has been used extensively to recapitulate the biochemical hallmarks of SLOS both *in vitro* and *in vivo* (Francis et al., 2016; Kolf-Clauw et al., 1996). U18666A, a noncompetitive inhibitor of DHCR24, was used to inhibit the final step in the Bloch pathway at nanomolar concentrations where it does not perturb cholesterol trafficking (Cenedella, 2009; Lu et al., 2015). A comparison of AY9944 (KR targeting) with U18666A (Bloch targeting) also provided access to structure-activity relationships. Specifically, DHCR7-mediated reduction of the C(7–8) double bond confers the linear cholesterol ring structure (Serfis et al., 2001), such that AY9944 causes accumulation of non-planar sterols. Conversely, DHCR24 inhibition leads to the accumulation of more rigid sterols as it prevents the DHCR24-mediated reduction of C(24–25) (Chen and Tripp, 2012). The 3-hydroxy-3-methylglutaryl-CoA (HMG-CoA) reductase inhibitor atorvastatin was used to inhibit the synthesis of cholesterol and other biosynthetic intermediates, whereas MβCD was used to acutely deplete sterols from the PM (Rodal et al., 1999; Subtil et al., 1999). Sterol content in HEK293T cells relative to LPDS controls was raised ~25% when cultured in fetal bovine serum (FBS) and reduced by ~50% with atorvastatin, AY9944, or MβCD.

AY9944 treatment effectively led to the predicted accumulation of 7DHC and zymostenol, whereas U18666A induced a mild accumulation of desmosterol (Figure 1B).

To monitor the effects of cholesterol homeostasis on CME, we used CRISPR-Cas9 gene editing to fluorescently tag clathrin light chain A (CLTA) in HEK293T by using our previously described approach (Figure S1A; Anderson et al., 2018; Scott et al., 2018). A pooled population of genome-edited cells was enriched by fluorescence-activated cell sorting (FACS) to create a homogeneous population of $CLTA^{mTq2+}$ cells, thereby mitigating any off-target effects that arise in clonal populations (Figures S1B and S1C). Live-cell confocal microscopy taken at midsection planes revealed dynamic PM budding and rapid trafficking of clathrin-$mTq2^+$ vesicles in LPDS cultured cells. All sterol-depleted conditions, exemplified by AY9944 treatment, lead to striking immobilization of clathrin vesicles at the PM despite ongoing intracellular transport (Video S1, panels 1–2). Trafficking deficits induced by AY9944 treatment were efficiently rescued by addition of cholesterol-loaded MβCD (MβCD-Chol) as observed by rapid redistribution of clathrin-$mTq2^+$ traffic from the PM, indicating that PM cholesterol alone is sufficient and essential for clathrin trafficking (Video S1, panel 3). This effect was rapid, restoring CME within minutes of MβCD-Chol addition and rendering $mTq2^+$-clathrin traffic indistinguishable from LPDS controls within 1 h (Video S1, panel 3). To exclude potential secondary effects from the lipophilic properties of cholesterol synthesis inhibitors, small molecules were administered in the presence of exogenous cholesterol, thereby minimizing endogenous synthesis (Wassif et al., 2005). Under these conditions, the cholesterol synthesis inhibitors did not produce clathrin trafficking deficits (Figure 1C).

To determine the extent of functional CME impairment, we used a high-content, non-biased quantitation imaging assay to analyze the internalization of fluorescently conjugated transferrin (Tfn) across sterol-depleted conditions. The degree of sterol depletion achieved with these inhibitors (Figure 1B), predicted the reduction in CME. Treatment with either AY9944, atorvastatin, or MβCD reduced both sterol abundance and Tfn internalization by approximately 50%. U18666A had a smaller effect (~20% reduction) on both sterol levels and CME (Figure 1D). Confocal optical sections taken at midplane also confirmed the inhibition of Tfn internalization (Figure 1E), as seen by the loss of Tfn-555-positive vesicles in the cytoplasm and localization to the PM. Although Tfn internalization was impaired, the high Tfn-555 signal from the PM suggests that the TfR also accumulated on the PM. Because CME was impaired regardless of the step of cholesterol synthesis inhibition or time of cholesterol depletion, we speculated that cholesterol depletion or decreased total sterol content was the major mediator of this phenomenon, rather than the accumulation of specific sterol precursors. A parallel comparison of sterol profiles by gas chromatography-mass spectrometry (GC-MS) and Tfn uptake as a function of inhibitor concentration demonstrated that CME activity was dependent on total sterol content (Figures 1F and 1G).

Recovery of CME traffic was also predicted by sterol abundance and availability. Addition of MβCD-Chol following sterol depletion with AY9944 rapidly restored both $mTq2^+$-clathrin traffic and Tfn internalization (Figure 2B, top). In contrast, clathrin-$mTq2^+$ vesicle trafficking required 6–12 h to normalize following the addition of FBS, indicating slowed lipoprotein (LDL)-derived cholesterol uptake and redistribution (Figure 2B, middle), likely

due to depressed CME-dependent LDL uptake (Davis et al., 1986). Clathrin-mTq2$^+$ vesicle trafficking also did not recover within 12 h upon AY9944 removal and LPDS addition, indicating the rate of CME rescue by endogenous cholesterol synthesis is much slower than either direct or LDL-dependent cholesterol uptake (Figure 2B, bottom). Feedback inhibition of 7DHC on the synthetic pathway may also limit sterol biosynthesis (Honda et al., 1998). Cellular sterol profiles corresponded with the resumption of CME (Figure 2C). Notably, incubation of AY9944-depleted cells with MβCD-Chol corrected cellular sterol profiles more completely than the availability of LDL-derived cholesteryl esters (Figure 2C), suggesting a greater efficacy and bioavailability of cholesterol supplementation independent of endocytic traffic. These rescue assays demonstrate a definitive requirement for an optimal concentration of cellular cholesterol to facilitate clathrin vesicle trafficking.

7DHC can compensate for cholesterol in facilitating CME

As SLOS leads to a significant accumulation of 7DHC (Irons et al., 1993; Tint et al., 1994), we wanted to directly address the ability of 7DHC to compensate for cholesterol in supporting CME. Rescue of aberrant clathrin trafficking following AY9944 treatment was evaluated by loading cholesterol or 7DHC directly to cellular membranes by using MβCD as a water-soluble carrier. Incubation with MβCD-7DHC efficiently rescued total sterol levels back to cholesterol-replete conditions, with 7DHC being the predominate form (~80% of total sterols) (Figure S2A). The addition of uncomplexed MβCD to cells already depleted of sterols did not further reduce sterol levels, which may reflect diminished “free” cholesterol available for MβCD exchange. Restoration of total sterol levels by either MβCD-Chol or MβCD-7DHC resulted in resumed clathrin-mTq2$^+$ trafficking (Video S2) and Tfn internalization (Figures S2B and S2C). This finding suggests that the loss of planarity within the sterol ring, due to the additional double bond in 7DHC (Serfis et al., 2001), does not impede its endocytic function at the membrane. Although 7DHC has been suggested to impact other aspects of PM structure, including bending rigidity (Gondré-Lewis et al., 2006) and lipid packing (Tulenko et al., 2006), our results demonstrate that 7DHC can compensate for cholesterol in sustaining CME. Thus, CME appears to be sensitive to total sterol content but robust to sterol identity.

Altered sterol homeostasis inhibits clathrin-coated pit dynamics and membrane bending

We predicted that cholesterol’s multifaceted influence on PM properties may contribute to membrane curvature generation and influence the recruitment of CME proteins. To determine how cholesterol and sterols influence membrane bending during clathrin assembly, we used polarized total internal reflection fluorescence microscopy (polTIRFM) of DiI, which allows imaging of PM topography (Aguet et al., 2013; Anantharam et al., 2010; Scott et al., 2018). Imaging of membrane bending in polTIRFM is achieved by selective excitation of DiI-labeled PM within the vertical (P polarization) or horizontal (S polarization) plane with respect to the coverslip and quantified by the ratio of P/S fluorescence (Anantharam et al., 2010). We previously demonstrated that this approach can accurately measure changes in membrane topography during membrane bending during CME by correlative light and electron microscopy (CLEM) and atomic force microscopy (CLAFM) (Scott et al., 2018). The membrane bending dynamics of individual endocytic events were recorded in SK-MEL-2 cells endogenously expressing clathrin-mTq2$^+$ and

dynamin-eGFP^{+} with DiI-labeled membranes (Video S3). CME dynamics of the SK-MEL-2 cell line have been well characterized by live-cell TIRFM and polTIRFM (Doyon et al., 2011; Scott et al., 2018).

Upon disruption of cholesterol homeostasis, total sterol content relative to LPDS culture was found to be 147% ± 24% (FBS), 81% ± 7% (atorvastatin), 82% ± 11% (AY9944), or 34% ± 9% (MβCD) in SK-MEL-2-treated cells (data not shown). Under all sterol deplete conditions (AY9944, atorvastatin, and MβCD), the total number of unique, distinct clathrin assembly spots per cell area over time was significantly lower relative to cells grown in complete media or LPDS (Figure 3C). Both moderate and severe sterol depletion led to an increase in the number of persistent clathrin tracks (>400 s) (Figure 3D) and average clathrin lifetimes per cell (Figure 3F). The accumulation of clathrin-mTq2^{+} spots with sterol depletion indicated that the reduction in clathrin tracks was not due to a lack of clathrin assembly but arrested CME (Video S4; Figure 3A). Clathrin-mTq2^{+} tracks were further categorized according to detection of dynamin and P/S signal. Although dynamin may contribute to early stages of clathrin-coated pit maturation (Aguet et al., 2013; Srinivasan et al., 2018), it is most abundant during membrane fission. Dynamin-eGFP^{+} was visualized as a burst of accumulation immediately prior to the completion of endocytosis and the disappearance of the clathrin-coated vesicle (Figure 3B). Using dynamin recruitment to clathrin-mTq2^{+} spots as a marker of completed (e.g., productive) CME events, we found that the number of productive CME events per cell area was dramatically reduced during sterol depletion (Figure 3E). When CME events did occur, they exhibited longer lifetimes than FBS or LPDS controls (Figure 3G; Figure S3). Following AY9944 treatment, the average lifespan of CME events that could be observed was increased by 40 s (95% confidence interval [CI] [89,148]) compared to those of LPDS controls (95% CI [66, 97]). CME lifetimes in AY9944-treated cells are underestimated by thse data due to temporal limitations in video tracking of persistent CME tracks. A detailed breakdown of clathrin lifetimes under control or sterol-depleted conditions is shown in Figure S4.

Although both moderate (AY9944 and atorvastatin) and severe (MβCD) cholesterol depletion led to diminished CME rates, we observed treatment-specific impacts on membrane curvature dynamics. Cells displaying ~20% reduction in total sterol content following AY9944 or atorvastatin treatment exhibited clathrin-mTq2^{+} spots associated with strong P/S signals, indicating the presence of highly curved pits that stalled prior to acquiring bursts of dynamin (Figure 3A). DMN2-eGFP^{+} localization was delayed in both AY9944- and atorvastatin-treated cells compared to LPDS controls, suggesting clathrin events inefficiently recruited dynamin and did not become productive CME events. As illustrated by kymographs of long-lived clathrin tracks failing to undergo scission (Figure S5), fluctuations in P/S membrane bending along clathrin tracks were noted. Although a weak DNM2^{eGFP+} signal was associated with many curved clathrin structures, robust dynamin signatures could also be seen dissociating without a loss of clathrin signal. No differences in dynamin lifetimes were observed in association with productive CME events (data not shown). These findings suggest that a moderate disruption of cholesterol synthesis allowed membrane bending during the early stages of CME but precluded neck formation and the recruitment of dynamin. In contrast, cells displaying ~65% reduction in total sterols following MβCD treatment exhibited diminished P/S signals with little to no dynamin

recruitment (Figures 3A and 3H), indicating that severe sterol depletion inhibits CME at initial membrane bending. This result is consistent with previous studies describing flat clathrin-coated structures following MβCD-mediated sterol depletion, consistent with an inability of clathrin-coated pits to invaginate (Rodal et al., 1999). Altogether, these findings suggest that a homeostatic level of cholesterol is required at multiple stages of PM bending for the CME pathway to proceed normally.

Sterol depletion inhibits curvature generation and neck formation during CME, producing an asymmetric pit structure

To quantitatively assess curvature, we performed platinum replica electron microscopy (EM) of unroofed SK-MEL-2 cells (Sochacki et al., 2014, 2017) and classified clathrin structures as flat, shallow, domed, or spherical (Figure 4B). In cholesterol replete conditions (FBS or LPDS culture), flat and spherical clathrin-coated pits were most commonly observed with fewer shallow or domed structures. This finding is consistent with a rapid progression of CME pits from flat to spherical, as described previously in FBS-cultured SK-MEL-2 cells (Scott et al., 2018). In contrast, moderate sterol depletion with atorvastatin or AY9944 increased the relative frequency of shallow and domed structures, predominately at the expense of spherical pits (Figure 4B). The increased frequency of shallow/domed structures explains the high P/S signal observed on clathrin spots by polTIRFM with AY9944 and atorvastatin treatment (Figure 3A). Combined with the fluctuations observed in the P/S signals (Figure S5), these findings suggest that the structural transition from shallow to domed morphology is metastable, potentially due to the energetics of clathrin-coat lattice reorganization competing with elevated free energy costs of membrane bending upon sterol depletion. Consistent with polTIRFM studies, severe sterol depletion by MβCD shifted the relative frequency of coated pit curvature to predominately flat or shallow pits, reinforcing the concept that sterol depletion from the PM increases the energetic cost of membrane bending (Figure 4A). Absolute values of the categorized clathrin structures per cell are summarized in Figure S6. In support of intrinsic membrane properties altering the energetics of membrane bending, caveolae under cholesterol deplete conditions also exhibited a flattened, disassembled morphology (Figure 4F) and were decreased in number at the PM (Figure 4G). These findings provide direct structural evidence that sterol abundance influences CME event progression by altering membrane bending dynamics at multiple stages of curvature generation.

Sterol depletion also resulted in the loss of pit structural symmetry. Although most clathrin structures in MβCD-treated cells were flat, the few observable spherical pits were asymmetric and distorted (Figure 4D), suggesting aberrant energetics of membrane bending. Upon sterol depletion with AY9944 or atorvastatin, distorted coated pits exhibiting elongated necks without a narrow base were observed (Figure 4D, inset), and asymmetry scaled with the severity of cholesterol depletion (Figure 4D). Aside from the numerous flat clathrin structures within MβCD treatment (Figure 4E, panel 1), no differences in the average size of clathrin structures were observed across treatments within the shallow, domed, and spherical subsets of curvature classification (Figure 4E, panels 2–4). This result suggests that once energetic barriers were crossed, general pit dimensions were constant. Notably, the area of the PM covered by clathrin increased dramatically from approximately

1.5% in FBS and LPDS controls to 3.0%, 4.0%, and 8.7% when treated with atorvastatin, AY9944, or MβCD, respectively (Figure 4C). A possible explanation for the loss of clathrin pit symmetry upon sterol depletion may be due to the accumulation of stalled pits on the PM resulting in asymmetric membrane bending trajectories during the remodeling of large, flat clathrin lattices into vesicles (Avinoam et al., 2015; Scott et al., 2018). These data demonstrate that perturbation of cholesterol homeostasis alters the process of clathrin assembly and the trajectory of membrane bending, leading to an accumulation of normal and distorted clathrin-coated pits on the PM.

Phase separation predicts the sterol structural requirements for supporting CME

To clarify the sterol structural requirements necessary to support CME, we used MβCD to deliver structurally diverse sterols and tested their ability to rescue CME function following AY9944 inhibition. As summarized in Figure 5A and Table S2, sterols were chosen based on differences in ring structure (lathosterol and 7DHC), aliphatic tail structure (desmosterol), and predicted ability to phase separate or support transbilayer movement of sterols. Cholestenone, which substitutes the 3β-hydroxyl with a ketone group as is typical of steroid hormones, likely diminishes polar interactions at the membrane-water interface to promote more rapid interleaflet exchange (Róg et al., 2008). Conversely, increased polarity (4β-hydroxycholesterol) or charge (cholesterol sulfate) would impede sterol exchange between membrane leaflets and do not support phase separation (Bacia et al., 2005; Wenz and Barrantes, 2003).

Incubation with desmosterol, 7DHC, lathosterol, or 4β-hydroxycholesterol MβCD-sterol complexes efficiently rescued total sterol levels to LPDS levels (Figure 5B). MβCD-cholesterol sulfate and cholestenone complexes only allowed for sterol exchange (total cellular sterol content remained near AY9944 levels). Sterols previously demonstrated to allow for sterol flipping and supporting phase separation (desmosterol and 7DHC) rescued Tfn internalization (Figures 5C and 5D). However, Tfn internalization was not rescued by sterols that do not support phase separation or allow membrane flip-flop (4β-hydroxycholesterol) (Figures 5C and 5D). This result suggests that sterol structures supporting phase separation confer similar requirements necessary to support CME.

Integrity of the actin cytoskeleton does not significantly modulate CME sterol dependence

During CME, the polymerization energy of the clathrin lattice is opposed by membrane bending energy (Saleem et al., 2015). Although the actin cytoskeleton is not a requirement for CME in mammalian cells, it becomes increasingly important as membrane tension increases (Batchelder and Yarar, 2010; Boulant et al., 2011). Actin polymerization is thought to provide additional force during the transition of domed- to spherical-shaped pits in preparation for vesicle scission (Grassart et al., 2014; Hassinger et al., 2017; Skruzny et al., 2012). To determine whether inhibition of CME by sterol depletion is mediated through actin cytoskeleton changes or specific to the membrane, we depolymerized actin with latrunculin B pre-treatment during inhibition by AY9944 or following recovery of CME activity by sterol repletion (Figure S7C). We did not find evidence of significant latrunculin B sensitivity in either restoring CME activity in sterol-depleted cells or inhibiting MβCD-cholesterol rescue (Figure S7E). These data suggest that the influence of sterols on

CME is largely independent of actin remodeling but directly dependent on changes to the physical properties of the PM.

Patient fibroblasts containing mutations within cholesterol synthesis genes exhibit functional CME deficits

To determine if CME activity was reduced within the context of a human disease characterized by sterol disruption, Tfn uptake assays were performed on fibroblasts derived from SLOS subjects. Three cell lines were selected to be representative of the SLOS disease spectrum (Table S3). Compared to an unaffected control, Tfn uptake was greatly reduced in SLOS samples upon culture under LPDS conditions (Figures 6A and 6D), which is similar to AY9944-treated controls. Although CME activity was similarly inhibited in all three SLOS fibroblasts when cultured under LPDS conditions, CME function correlated to the total sterol levels of each cell line as determined by GC-MS (Figure 6B). Notably, even under cholesterol replete conditions, fibroblasts from the most biochemically severe SLOS cell lines trended toward diminished Tfn internalization, suggesting that exogenous lipid supplementation is unable to fully rescue CME function (Figure 6C). These data demonstrate a direct link between sterol homeostasis and CME within SLOS subjects and suggest functional deficits in CME may have clinical impact within this population.

DISCUSSION

Here, we present evidence for the role of sterols in aiding membrane curvature generation during CME by direct observation of alterations in membrane-bending dynamics. Our findings suggest that cholesterol is relevant to multiple stages of PM bending during an endocytic event, which is consistent with a structural role in alleviating energetic stress. Rescue of trafficking deficits by sterol substitution suggests that the structural requirements for CME mirror the sterol requirements for supporting L_o domain formation or minimally lipid packing capacity (Megha et al., 2006; Wenz and Barrantes, 2003). This idea agrees with endocytosis requiring the sterol 3β-hydroxyl group and sterol support of ordered domain formation (Kim et al., 2017). In our hands, desmosterol behaved most similarly to cholesterol while strongly raft promoting sterols 7DHC and lathosterol compensated for cholesterol to a lesser degree. Although this observation does not imply stable PM rafts or exclude regulation of membrane protein effectors, it is notable given the body of work implicating membrane phase separation within curved membranes and budding theory (Bacia et al., 2005; Bruckner et al., 2009; Hilgemann et al., 2020; Huttner and Zimmerberg, 2001; Jülicher and Lipowsky, 1993, 1996). During CME progression, a high energetic cost is associated with the initiation of membrane bending and is problematic for vesicle neck formation (Lentz et al., 2002). Although the impact of cholesterol on membrane rigidity (Henriksen et al., 2004; Song and Waugh, 1993) may appear contradictory to its observed effect in facilitating membrane curvature, cholesterol's negative spontaneous curvature (Chen and Rand, 1997) and localization to sites of correspondingly negative curvature will reduce the curvature energy. Generally, a leaflet with a mixture of lipids with various spontaneous curvatures has a softer bending modulus (Leibler, 1986). Furthermore, molecular simulations indicate that the formation of an ordered phase by cholesterol favors positive curvature (Sodt et al., 2016). Thus, we propose that cholesterol is supporting highly

curved structures along the endocytic path, depending on the leaflet lipid composition and external forces that are driving the curvature (Figure 7). Biophysical studies in artificial membranes suggest that cholesterol flip-flop may relax tension in L_o domains despite their increased stiffness (Bacia et al., 2005; Bruckner et al., 2009), explaining why lipid rafts may be preferential sites for membrane budding and endocytosis (Conner and Schmid, 2003; Huttner and Zimmerberg, 2001). Although it is possible that cholesterol could contribute to CME through a previously unrecognized lipid-sensing or signaling mechanism, demonstrated CME sensitivity to sterol abundance at multiple stages of curvature generation and robustness to sterol identity support a mechanical mechanism of sterol-mediated membrane relaxation.

In addition to modifying membrane bilayer architecture directly, sterol homeostasis may also impact CME through secondary mechanisms. Membrane curvature itself may influence the intrinsic activity of enzymes involved in membrane traffic (Bozelli et al., 2018). Recruitment of curvature-sensing structural proteins may also be affected, including ENTH/ANTH and BAR domain proteins that promote PM curvature through scaffolding or hydrophobic insertion (Haucke and Kozlov, 2018). Cholesterol's influence on lateral packing and ordering of the local lipid environment may also disrupt $PI(4,5)P_2$ organization (Kwik et al., 2003), which may affect the association of PH-domain-containing CME proteins. Packing of cargo is likely less affected by sterol depletion, as the concentration of TfR was shown to increase in accordance with coated pit surface area (Rodal et al., 1999). Although not required for CME in mammalian cells, actin assembles during the final stages of CME to aid in the transition of domed- to spherical-shaped pits and vesicle scission under conditions of increased membrane tension (Boulant et al., 2011; Hassinger et al., 2017; Skruzny et al., 2012). Although disruption of actin integrity did not change CME responses to the disruption of sterol synthesis, acute cholesterol depletion with MβCD is known to lead to stabilization of the actin cytoskeleton and increase membrane-cytoskeleton adhesions (Khatibzadeh et al., 2012). Given that the balance between endocytosis/exocytosis and the cytoskeleton is highly coordinated through membrane tension (Diz-Muñoz et al., 2013), a holistic understanding of membrane surface dynamics in response to cholesterol depletion may lead to a more cohesive understanding of cellular responses and those observed within SLOS (Jiang et al., 2010).

As our findings favor a biophysical rather than biochemical role for cholesterol in facilitating membrane curvature, we predict our findings may extend to other endocytic and membrane remodeling processes. Other endocytic pathways, including caveolar, clathrin-independent, macropinocytosis, and clathrin- and caveolae/caveolin1-independent endocytosis, are known to be sensitive to cholesterol depletion (Doherty and McMahon, 2009). We observed flattened and disassembled caveolar structures, consistent with previous work (Rothberg et al., 1990, 1992) and reports that caveolin-1 may sense and induce membrane curvature by cholesterol clustering (Krishna and Sengupta, 2019). Cholesterol also appears to be necessary for fusion pore kinetics during exocytosis in platelets (Ge et al., 2010), chromaffin cells (Wang et al., 2010), and neurons (Najafinobar et al., 2016). In the few studies in which endocytosis and exocytosis have been measured simultaneously, sterol depletion principally impairs endocytosis (Subtil et al., 1999; Yue and Xu, 2015). Intracellular recycling of TfR to the cell surface also appeared to be unaffected, suggesting

the PM may be more susceptible to sterol depletion than other intracellular compartments (Subtil et al., 1999). A plausible explanation may lie in the transbilayer asymmetry of PM sterol distribution and directionality of sterol flux, as lipid gradients maintained across organelles have been proposed to provide self-organizing directionality to both secretory and endosomal pathways (Levental et al., 2020).

Our studies suggest that reduced endocytic activity may contribute to the cellular phenotypes observed within SLOS, potentially providing an explanation for some of the tissue-specific abnormalities reported within SLOS. As endocytosis and exocytosis are functionally coupled, CME impairment may be linked to trafficking abnormalities described within secretory granules of the pancreas and pituitary and adrenal glands in *Dhcr7*$^{-/-}$ mice (Gondré-Lewis et al., 2006). Impaired endocytic traffic may also lead to endosomal-lysosomal dysregulation, possibly related to both aberrant Sonic hedgehog signaling (Blassberg and Jacob, 2017; Blassberg et al., 2016) and compromised phagosome maturation (Futter et al., 2012; Ramachandra Rao et al., 2018). During embryonic development, CME is necessary for the maintenance of pluripotency through regulation of pluripotent and differentiation signals (Narayana et al., 2019). Impaired Wnt/β-catenin and cadherin-related signaling was recently identified within SLOS-patient-derived stem cells (Francis et al., 2016), suggesting a role for CME deficits within cell fate and developmental pathologies. Within the nervous system, dynamic communication between neurons is highly dependent upon vesicular trafficking and CME for rapid neurotransmission, receptor desensitization, dendritic spine plasticity, and myelination (Murthy and Stevens, 1998; Saheki and De Camilli, 2012; Watanabe et al., 2014; Winterstein et al., 2008). Interestingly, impairment of CME through *DNM1* mutations causes epileptiform discharges (Dhindsa et al., 2015), a prevalent finding in SLOS subjects (Schreiber et al., 2014). Rapid endocytosis is also of significant relevance to the brush boarder of small intestinal enterocytes whose microvilli exhibit high curvature and are highly enriched in cholesterol (Hansen et al., 2003; Huttner and Zimmerberg, 2001). Endocytic deficits could contribute to feeding difficulties and gastrointestinal intolerance observed in SLOS. Reduced TfR-mediated internalization may explain the observed increased levels of Tfn protein present within the retina of AY9944-treated rats (Tu et al., 2013) and cerebrospinal fluid of SLOS subjects (Cologna et al., 2016). Cholesterol's complex role in different cellular functions indicates that malformations and functional deficits observed within disorders of cholesterol synthesis could be due to competing and disparate effects of the lipid. The extent to which the impairment of CME contributes to disease pathogenesis and clinical phenotypes observed will thus require further study.

Current treatment strategies for SLOS include empirical dietary cholesterol supplementation, which was shown to normalize plasma cholesterol with variable outcomes on sterol precursors (Linck et al., 2000). However, cholesterol supplementation does not universally correct plasma cholesterol concentrations and plasma cholesterol does not necessarily reflect tissue sterol content. Furthermore, the benefits of dietary cholesterol supplementation have been modest (Svoboda et al., 2012), and longitudinal studies indicate that baseline cholesterol levels are a better predictor of developmental trajectory (Sikora et al., 2004). Depressed CME activity may be linked to suboptimal cholesterol bioavailability. Our studies indicate that once CME is inhibited by AY9944, clathrin trafficking requires 6–12 h to

resume in the presence of FBS and yet recovers within minutes by direct delivery of MβCD-Chol. Interestingly, a secondary defect in LDL metabolism was described in SLOS fibroblasts, in which decreased LDL apolipoprotein degradation products were observed (Wassif et al., 2002). Although this mechanism likely involves impaired NPC1 function (Wassif et al., 2002), a defect in LDL internalization due to impaired CME efficiency may also contribute. A potential strategy to overcome impaired internalization and utilization of cholesterol *in vivo* is the direct delivery of cholesterol by a mechanism independent of receptor-mediated endocytosis, such as a CD carrier. This approach could preferentially target PM properties mediating CME impairment and bypass impaired lysosomal function necessary for the liberation of cholesterol esters. Our sterol substitution studies also indicate that cholesterol precursors are more readily mobilized by MβCD, with cholesterol preferentially retained. CD-mediated cholesterol delivery may thus aid in sterol precursor clearance. CDs have been widely studied (Vecsernyés et al., 2014) and have received phase II and III regulatory approval for the treatment of Niemann-Pick disease type C1 (Ory et al., 2017). A reversal of this strategy as a cholesterol delivery mechanism in SLOS may overcome hindrances to cholesterol supplementation therapy.

In summary, we find that the maintenance of cholesterol homeostasis is essential for efficient clathrin-mediated endocytosis, demonstrate an active role for sterols in mediating membrane remodeling during this process, and provide mechanistic detail into the sterol functional requirements necessary for this process. Although the extent to which altered CME dynamics and function contribute to the pathogenesis of disorders of cholesterol metabolism is unclear, further investigation into CME's role within these orphan diseases is warranted.

STAR★METHODS

RESOURCE AVAILABILITY

Lead contact—Further information and requests for resources and reagents should be directed to and will be fulfilled by the Lead Contact, Kevin Francis (kevin.francis@sanfordhealth.org).

Materials availability—All unique/stable reagents generated in this study are available form the Lead Contact with a completed Materials Transfer Agreement.

Data and code availability

- All data reported in this paper will be shared by the Lead Contact upon request.
- This paper does not report original code.
- Any additional information required to reanalyze the data reported in this paper is available from the Lead Contact upon request.

EXPERIMENTAL MODEL AND SUBJECT DETAILS

Cell culture—HEK293T (parental and hCLTA^{EN}-Tq2) and human SK-MEL-2 (hCLTA^{EN}-Tq2 hDNM2^{EN}-eGFP, as previously described; Scott et al., 2018) were maintained in

DMEM (GIBCO, 4.5 g/L glucose, 110 mg/L pyruvate), supplemented with 10% (v/v) FBS (Hyclone), and 1,000 U/mL penicillin/streptomycin. For inhibition of cholesterol synthesis, cells were rinsed twice in serum-free DMEM and cultured under cholesterol deplete conditions in 7.5% delipidated serum (LPDS) for 48 h with small molecule inhibitors AY9944 (2.5 μM, Cayman Chemical; *DHCR7* inhibitor), U18666A (20 nM, Cayman Chemical; *DHCR24* inhibitor), Atorvastatin (1 μM, Cayman Chemical), or Simvastatin (Cayman Chemical), or at concentrations as otherwise specified. Acute sterol depletion was achieved by 1 h incubation with 5 mM MβCD (Alfa Aesar, 1303.31 g/mol) at 37°C. De-identified fibroblasts cultured from skin punch biopsies from Smith-Lemli-Opitz subjects (kind gift from Dr. Forbes Porter, NICHD) were maintained in DMEM (GIBCO, 4.5 g/L glucose, 110 mg/L pyruvate), supplemented with 15% (v/v) FBS (Hyclone), and 1,000 U/mL penicillin/streptomycin. SLOS fibroblasts were rinsed twice in serum-free DMEM and cultured for 10 days in 7.5% (v/v) LPDS to induce biochemical profiles. SLOS fibroblast cells lines were described previously (Krakowiak et al., 2000; Wassif et al., 1998).

CRISPR/Cas9 gene editing of clathrin light chain—C' terminal targeting of the *CLTA* gene to enable fluorescence tracking with mTuroquise2 (mTq2) was performed using a homology-directed repair strategy as previously described (Anderson et al., 2018; Scott et al., 2018). Briefly, a guide RNA (5′-GCAGATGTAGTGTTTCCACA-3′) targeting the open reading frame in the immediate vicinity of the stop codon was cloned into the Cas9 expression vector pX330-U6-Chimeric_BB-CBh-hSpCas9 (gift from Feng Zhang; Cong et al., 2013), Addgene plasmid #42230). The donor vector consisted of 1 kB homology arms flanking a cassette containing puromycin N-acetyl-transferase expressed in-frame with *CLTA* and Tq2 via the self-cleavable peptide sequence P2A. 1×10^6 HEK293T cells were transfected with 4 μg donor and 2.5 μg pX330 Cas9 plasmid (CalPhos™ Mammalian Transfection kit, Clontech). After 72 h, Tq2 positive cells were isolated with a FACSJazz Cell Sorter (BD Biosciences) and characterized as described previously (Figure S1; Anderson et al., 2018).

METHOD DETAILS

Preparation of lipoprotein-deficient serum—To facilitate cell culture under defined lipid conditions, fetal bovine serum (FBS) devoid of sterols, triglycerides, and other neutral lipids was prepared based on previously described techniques (Cham and Knowles, 1976). To prevent oxidation due to trace peroxides, 0.1 mg ethylenediamine tetraacetate (EDTA) was added per 50 mL FBS. Serum was mixed 1:2 with organic phase (consisting of 3:2 ratio diisopropyl ether:n-butanol) followed by vigorous stirring for 1 h protected from light. After centrifugation at 4°C for 15 min at 2200 rpm, the aqueous layer was collected and lyophilized. Following resuspension in molecular grade H_2O, ITS-G supplement (Invitrogen) was added, the solution filter-sterilized, and stored at −20°C. GC-MS analysis indicated nearly undetectable cholesterol levels. Lipoprotein-deficient, delipidated serum (LPDS) was substituted for regular FBS to stimulate expression of *de novo* cholesterol biosynthesis.

Sterol loading of MβCD—Methyl-β-cyclodextrin (MβCD)-cholesterol complex commercially available (Sigma, C4951). For MβCD-sterol complexation, 50 mg/mL sterol

stocks in 1:1 chloroform:methanol were prepared for desmosterol, lathosterol, cholestenone, cholesterol sulfate, 4β-hydroxycholesterol (Avanti Polar Lipids), 7DHC and cholesterol (Sigma or Avanti Polar Lipids). Stoichiometry of MβCD-cholesterol complexes typically consists of one cholesterol molecule entrapped within two CDs (1:2 molar ratio). We found optimal loading conditions using a 1:7 molar ratio, where desired sterol concentration was dried under nitrogen flow, followed by addition of 5 mM MβCD (Alfa Aesar, 1303.31 g/mol) prepared in serum-free DMEM. Sterol suspensions were sonicated for 5 min and incubated at 37°C with agitation overnight. Sterol crystals were subsequently removed via 0.45 μm filtration. Sterol loading rescue experiments were performed by incubation for 1 h at 37°C supplemented with 0.5% BSA, followed by removal and addition of 7.5% LPDS for imaging or subsequent analysis to limit prolonged exposure to MβCD. Comparison of the physical properties and phase separation behavior of sterols was previously described (Bacia et al., 2005; Keller et al., 2004; Megha et al., 2006; Wenz and Barrantes, 2003).

GC-MS sterol analysis—Cell pellets flash frozen on dry ice were reconstituted in 1 mL of water and lysed by successive freeze/thaw cycles in a 50°C bead bath. 50 μL per sample was removed for protein quantification (MicroBCA Protein Assay, Pierce Biotechnology). 1 mL saponification buffer containing 7% KOH in 92% ethanol with 10 ug/mL coprostan-3-ol (Sigma) was added to 900 μL cell lysate. Following saponification at 60°C for 1 h, an additional 1 mL of water was added to each sample and the aqueous phase extracted with 3 mL ethyl acetate by vortexing and centrifugation at 2200 rpm. The organic phase was then extracted with 2 mL water, concentrated to dryness by heating at 50°C under nitrogen flow, residue dissolved in 50 μL pyridine (CHROMASOLV Plus, Sigma), and sterols derivatized in 50 μL N,O-bis(trimethylsilyl) trifluoroacetamide with 1% trimethylchlorosilane (BSTFA + 1% TMCS, Thermo Fisher TS-38831) at 60°C for 1 h. Sterol levels were determined by GC-MS analysis as previously described (Kelley, 1995). Samples were analyzed by automatic injection of 1 μL of the derivatized sterol mixture into an Agilent 7890 GC using a split injection port (4 mm ID × 78.5 mm quartz wool liner, Restek 23309) leading to a 0.18 mm ID × 20 m 1,4-bis(dimethylsiloxy)phenylene dimethyl polysiloxane column (Restek, 43602). Helium was used as a carrier gas at a linear rate of 46.9 cm/sec. After 0.5 min at 170°C, the oven temperature was raised to 250°C at 18°C/min, then to 280°C at 3°C/min, and finally to 320°C at 20°C/min and held for 7 min. An Agilent 5977B mass spectrometer was operated in the electron impact mode at 70 eV with an ion source temperature of 275°C.

Transferrin uptake assay—HEK293T cells were plated onto 0.1% gelatin coated 12 mm coverslips or 96 well glass bottom plates (Cellvis) and treated for 48 h under respective treatment conditions. For AY9944 rescue experiments, cells were placed in DMEM/BSA (DMEM containing 0.5% w/v BSA; bovine serum albumin) alone or DMEM/BSA containing 5 mM MβCD-sterol complexes for 1 h in a 37°C humidified incubator containing 5% CO_2. HEK293T cells were then incubated with transferrin (Tfn) conjugated to Alexa Fluor™ 555 (25 ug/mL, Invitrogen) for 30 mins at 37°C, followed by rinsing in ice-cold PBS, and fixation in 4% paraformaldehyde for 20 min. For high-content imaging analysis, 24 well glass bottom plates (Cellvis) were imaged using CX7 Rescue High-Content Screening (HCS) Navigator software (PerkinElmer, Waltham, MA) and standard HCS imaging protocol.

Patient fibroblasts were plated onto 0.1% gelatin coated 12 mm coverslips 3 days prior to imaging. Uptake was performed as described above using Tfn conjugated to Alexa Fluor™ 555 (25 ug/mL, Invitrogen) for 15 min at 37°C. Following incubation, cells were rinsed with ice-cold PBS. Cells were fixed in 4% paraformaldehyde for 20 min, rinsed three times in PBS, and mounted onto glass slides with Dako mounting media (Agilent). Cell outlines were traced using the freehand selection tool and the integrated density of 25 cells from 8–12 fields was quantified using ImageJ software (v1.8.0).

Actin network integrity was assessed by treatment of HEK293T cells with 50–400 nM latrunculin B (LatB, Calbiochem) at 37°C as described (please reference Figure S7 legend). Cultured cells were pretreated with 250 nM LatB for 30 mins prior to a 1 hour sterol repletion with MβCD-Chol and 30 min incubation with Tfn conjugated to Alexa Fluor™ 555 (25 ug/mL, Invitrogen). The cells were maintained in LatB during the sterol exchange and incubation with conjugated Tfn and compared to LatB washout controls.

Confocal microscopy—Images were captured using a Nikon A1R resonant scanning multispectral confocal microscope (Nikon Instruments, Inc. Melville, NY), equipped with a live cell chamber (37°C with humidified 5% CO_2), Nikon Ti Perfect Focus system, and NIS-Elements analysis software (Nikon). 48 h prior to live-cell imaging, HEK293T cells plated onto 0.1% gelatin-coated FluoroDish™ culture plates (35 mm, World Precision Instruments Inc.) were rinsed twice with DMEM (GIBCO) to remove residual lipids and respective treatments were added. Prior to imaging, culture media was refreshed. Time-lapse videos were obtained at 100x magnification (1.45 NA oil objective) at 5–20 s intervals over a 5 min duration.

Polarized TIRF microscopy—SK-MEL-2 hCLTA^{EN}-Tq2 hDNM2^{EN}-eGFP cells were seeded onto fibronectin-coated (Corning) 25 mm coverslips at a density of 8.0×10^4 cells/cm^2 and imaged within 4–6 hours of plating. To facilitate membrane labeling, a fresh DiI (1,1'-Dioctadecyl-3,3,3′,3′-teramethylindocarboncyanine perchlorate) solution containing 1 μg/mL DiI in 2.5% DMSO/HBSS (Corning) was prepared for each coverslip from a 1 mg/mL DiI stock dissolved in DMSO and stored under nitrogen. After incubating the freshly prepared DiI solution at 37°C for 5 min, 200–300 μL was added dropwise to coverslips containing 1 mL HBSS. Cells were labeled for 20 s with gentle pipetting, rinsed three times in HBSS, and placed into imaging buffer. Imaging buffer for all treatment conditions consisted of Leibovitz's L-15 media supplemented with either 10% FBS or delipidated (LPDS) serum (Hyclone) to monitor basal CME events. Following DiI labeling, coverslips were immediately imaged for no more than 45 min. To ensure consistency in DiI labeling, only cells with mean S polarization intensities between 350–800 were included in the analysis.

TIRFM images were captured on a custom built Till iMic (Till Photonics, Germany) inverted microscope outfitted with a 60x/1.49 NA oil immersion objective and environmental chamber kept at 37°C as previously detailed (Scott et al., 2018). In brief, excitation for mTurquise2, eGFP, and polTIRF was achieved by 445 (470/22), 488 (510/10), 561 (595/50) nm lasers respectively, collected on three EMCCD cameras (iXon3 885, Andor Technology). Back focal plane centering was performed daily to optimize the incidence angle using

MATLAB analysis to map the angles of TIRF reflectance and determine mirror angle adjustments to center the optical plane. 2-point TIRF illumination facilitated polarization of the 561 nm laser to enable monitoring of membrane curvature. Focused excitation at 90° and 270° positions preferentially excite vertically oriented, DiI-labeled membrane (P polarization), while excitation at positions 0° and 180° selectively excite horizontally labeled membrane (S polarization).

Transmission electron microscopy—SK-MEL-2 cells were prepared as described for polTIRF imaging by seeding onto fibronectin-coated 25 mm coverslips and allowed to adhere for 5 h. Coverslips were transferred into 2 mL stabilization buffer (70 mM KCl, 5 mM $MgCl_2$, 3 mM EGTA, 30 mM HEPES, pH 7.4) prior to unroofing with a 10 mL syringe and 22 gauge, 1.5 in needle containing 2 mL 4% PFA (Electron Microscopy Sciences) diluted in stabilization buffer. Coverslips were transferred to fresh 2% PFA/stabilization buffer and allowed to fix at RT for 20 min. Coverslips were mounted in 2% glutaraldehyde and sealed with VALAP (1:1:1 vasoline, lanolin, paraffin) for shipping. Sample preparation and TEM imaging of platinum cell membrane replicas was performed as previously described (Sochacki et al., 2014, 2017). Representative full EM images available upon request.

QUANTIFICATION AND STATISTICAL ANALYSIS

Sterol quantification by GC-MS—GC-MS analysis was performed using MassHunter software. Identification of TMS ethers of natural sterols was determined through comparison to commercially available standards for cholesterol, 7DHC, lathosterol, and desmosterol (Avanti Polar Lipids, Inc.), as well as comparison to MS spectra through the National Institute of Standards and Technologies Standard Reference Database when available. Identification of 8DHC was inferred as an isomer of 7DHC and comparison to SLOS fibroblasts; zymostenol identification was based on spectra from Conradi-Hünermann-Happle syndrome (CDPXD2) fibroblasts. Retention times and mass to charge (*m/z*) ratios are summarized in Table S1. Representative MS fragmentation patterns available upon request. TMS derivatives of sterols exhibiting abundance < 3% were excluded from analysis. For peak quantitation, sterol abundance was normalized to both the internal standard (coprostanol) and protein concentration. Data is presented relative to control samples using GraphPad Prism software.

Polarized TIRFM image analysis—Image registration was performed to align Turquoise2 and eGFP channels onto the polTIRF channel. Calibration images of fluorescent beads on a glass coverslip were acquired simultaneously on all three detectors and used to determine the geometric transformation during pre-processing. Bias images, acquired by capturing images with a closed shutter, were subtracted from each frame of the raw data. Using MATLAB, detection and tracking of fluorescence over time was performed using a modified version of cmeAnalysis software (Aguet et al., 2013) and custom scripts were used for association and classification of mTq2, eGFP, and P/S events (Scott et al., 2018). Modifications were made to adapt the software for our imaging system. Please contact authors for additional details. Detection criteria included a clathrin peak SNR > 4, dynamin SNR > 2, clathrin lifetime > 7 s, and a buffer of two consecutive frames before and after

each clathrin track. Faulty tracks were filtered from the analysis due to clathrin events crossing paths with another track and curvature signal unrelated to the tracked clathrin event itself. Frequency of clathrin tracks observed associated with curvature generation were classified as flat clathrin tracks, curved clathrin events, or curved CME events. Flat clathrin tracks were classified as exhibiting neither curvature nor dynamin recruitment, may represent persistent tracking or abortive clathrin events visiting the TIRM field. Curved clathrin events were classified as exhibiting positive P/S curvature signal, but failed to recruit dynamin. Curved CME events were classified by the ability of clathrin positive events to recruit dynamin.

Statistical analysis—All statistical analysis was performed using GraphPad Prism 8.0.2 (GraphPad Software, Inc., CA, US). Homogeneity of variances was tested by the Brown-Forsythe test. In cases of equal variances, data was analyzed by one-way ANOVA and post hoc Dunnett t test for multiple comparisons relative to LPDS control group. In cases of unequal variances, Welch ANOVA and post hoc Dunnett's T3 test was performed. $p < 0.05$ was accepted as significant. *, $p < 0.05$; **, $p < 0.01$; ***, $p < 0.001$; ****, $p < 0.0001$. Statistical details for each experiment can be found within figure legends.

Supplementary Material

Refer to Web version on PubMed Central for supplementary material.

ACKNOWLEDGMENTS

We thank Dr. Alexander Sodt (NIH/NICHD) for critical reading of this manuscript and insightful contributions to the biophysical mechanisms discussed. This study was supported by NIH grants (NIGMS P20 GM103620 and P20 GM103548). A.D.H. was supported by the National Science Foundation (0953561), a National Science Foundation/EPSCoR Cooperative Agreement (IIA-1355423), and the State of South Dakota through BioSNTR, a South Dakota Research Innovation Center. K.A.S. and J.W.T. were supported by the Intramural Research Program of the National Heart Lung and Blood Institute, National Institutes of Health (ZIA HL006098). R.H.A. was supported by the National Institutes of Health under a Ruth L. Kirschstein Fellowship (F30 NS106788). M.M.S. was supported by the Sanford Program for Undergraduate Research (P20 GM103620). We would like to thank the University of South Dakota Center for Brain and Behavior Research, the Sanford Imaging core, the Sanford Flow Cytometry core, and the NHLBI electron microscopy facility for support. Any opinions, findings, and conclusions or recommendations expressed in this material are those of the author(s) and do not necessarily reflect the views of the National Science Foundation or the National Institutes of Health.

REFERENCES

Aguet F, Antonescu CN, Mettlen M, Schmid SL, and Danuser G (2013). Advances in analysis of low signal-to-noise images link dynamin and AP2 to the functions of an endocytic checkpoint. Dev. Cell 26, 279–291. [PubMed: 23891661]

Anantharam A, Onoa B, Edwards RH, Holz RW, and Axelrod D (2010). Localized topological changes of the plasma membrane upon exocytosis visualized by polarized TIRFM. J. Cell Biol 188, 415–428. [PubMed: 20142424]

Anderson RH, Kerkvliet JG, Otta JJ, Ross AD, Leiferman PC, Hoppe AD, and Francis KR (2018). Generation of a CLTA reporter human induced pluripotent stem cell line, CRMi001-A-1, using the CRISPR/Cas9 system to monitor endogenous clathrin trafficking. Stem Cell Res. (Amst.) 33, 95–99.

Avinoam O, Schorb M, Beese CJ, Briggs JA, and Kaksonen M (2015). ENDOCYTOSIS. Endocytic sites mature by continuous bending and remodeling of the clathrin coat. Science 348, 1369–1372. [PubMed: 26089517]

Ayee MA, and Levitan I (2016). Paradoxical impact of cholesterol on lipid packing and cell stiffness. Front. Biosci 21, 1245–1259.

Bacia K, Schwille P, and Kurzchalia T (2005). Sterol structure determines the separation of phases and the curvature of the liquid-ordered phase in model membranes. Proc. Natl. Acad. Sci. USA 102, 3272–3277. [PubMed: 15722414]

Batchelder EM, and Yarar D (2010). Differential requirements for clathrin-dependent endocytosis at sites of cell-substrate adhesion. Mol. Biol. Cell 21, 3070–3079. [PubMed: 20631253]

Blassberg R, and Jacob J (2017). Lipid metabolism fattens up hedgehog signaling. BMC Biol. 15, 95. [PubMed: 29073896]

Blassberg R, Macrae JI, Briscoe J, and Jacob J (2016). Reduced cholesterol levels impair Smoothened activation in Smith-Lemli-Opitz syndrome. Hum. Mol. Genet 25, 693–705. [PubMed: 26685159]

Boulant S, Kural C, Zeeh JC, Ubelmann F, and Kirchhausen T (2011). Actin dynamics counteract membrane tension during clathrin-mediated endocytosis. Nat. Cell Biol 13, 1124–1131. [PubMed: 21841790]

Bozelli JC Jr., Jennings W, Black S, Hou YH, Lameire D, Chatha P, Kimura T, Berno B, Khondker A, Rheinstädter MC, and Epand RM (2018). Membrane curvature allosterically regulates the phosphatidylinositol cycle, controlling its rate and acyl-chain composition of its lipid intermediates. J. Biol. Chem 293, 17780–17791. [PubMed: 30237168]

Bruckner RJ, Mansy SS, Ricardo A, Mahadevan L, and Szostak JW (2009). Flip-flop-induced relaxation of bending energy: implications for membrane remodeling. Biophys. J 97, 3113–3122. [PubMed: 20006948]

Bucher D, Frey F, Sochacki KA, Kummer S, Bergeest JP, Godinez WJ, Kräusslich HG, Rohr K, Taraska JW, Schwarz US, and Boulant S (2018). Clathrin-adaptor ratio and membrane tension regulate the flat-to-curved transition of the clathrin coat during endocytosis. Nat. Commun 9, 1109. [PubMed: 29549258]

Cenedella RJ (2009). Cholesterol synthesis inhibitor U18666A and the role of sterol metabolism and trafficking in numerous pathophysiological processes. Lipids 44, 477–487. [PubMed: 19440746]

Chakraborty S, Doktorova M, Molugu TR, Heberle FA, Scott HL, Dzikovski B, Nagao M, Stingaciu LR, Standaert RF, Barrera FN, et al. (2020). How cholesterol stiffens unsaturated lipid membranes. Proc. Natl. Acad. Sci. USA 117, 21896–21905. [PubMed: 32843347]

Cham BE, and Knowles BR (1976). A solvent system for delipidation of plasma or serum without protein precipitation. J. Lipid Res 17, 176–181. [PubMed: 818332]

Chen Z, and Rand RP (1997). The influence of cholesterol on phospholipid membrane curvature and bending elasticity. Biophys. J 73, 267–276. [PubMed: 9199791]

Chen C, and Tripp CP (2012). A comparison of the behavior of cholesterol, 7-dehydrocholesterol and ergosterol in phospholipid membranes. Biochim. Biophys. Acta 1818, 1673–1681. [PubMed: 22465065]

Choubey A, Kalia RK, Malmstadt N, Nakano A, and Vashishta P (2013). Cholesterol translocation in a phospholipid membrane. Biophys. J 104, 2429–2436. [PubMed: 23746515]

Cocucci E, Aguet F, Boulant S, and Kirchhausen T (2012). The first five seconds in the life of a clathrin-coated pit. Cell 150, 495–507. [PubMed: 22863004]

Collins A, Warrington A, Taylor KA, and Svitkina T (2011). Structural organization of the actin cytoskeleton at sites of clathrin-mediated endocytosis. Curr. Biol 21, 1167–1175. [PubMed: 21723126]

Cologna SM, Shieh C, Toth CL, Cougnoux A, Burkert KR, Bianconi SE, Wassif CA, and Porter FD (2016). Altered cerebrospinal fluid proteins in Smith-Lemli-Opitz syndrome patients. Am. J. Med. Genet. A 170, 2060–2068. [PubMed: 27148958]

Cong L, Ran FA, Cox D, Lin S, Barretto R, Habib N, Hsu PD, Wu X, Jiang W, Marraffini LA, and Zhang F (2013). Multiplex genome engineering using CRISPR/Cas systems. Science 339, 819–823. [PubMed: 23287718]

Conner SD, and Schmid SL (2003). Regulated portals of entry into the cell. Nature 422, 37–44. [PubMed: 12621426]

Cunniff C, Kratz LE, Moser A, Natowicz MR, and Kelley RI (1997). Clinical and biochemical spectrum of patients with RSH/Smith-Lemli-Opitz syndrome and abnormal cholesterol metabolism. Am. J. Med. Genet 68, 263–269. [PubMed: 9024557]

Danino D, Moon KH, and Hinshaw JE (2004). Rapid constriction of lipid bilayers by the mechanochemical enzyme dynamin. J. Struct. Biol 147, 259–267. [PubMed: 15450295]

Das A, Goldstein JL, Anderson DD, Brown MS, and Radhakrishnan A (2013). Use of mutant 125I-perfringolysin O to probe transport and organization of cholesterol in membranes of animal cells. Proc. Natl. Acad. Sci. USA 110, 10580–10585. [PubMed: 23754385]

Davis CG, Lehrman MA, Russell DW, Anderson RG, Brown MS, and Goldstein JL (1986). The J.D. mutation in familial hypercholesterolemia: amino acid substitution in cytoplasmic domain impedes internalization of LDL receptors. Cell 45, 15–24. [PubMed: 3955657]

de Duve C (1971). Tissue fraction-past and present. J. Cell Biol 50, 20. [PubMed: 19866786]

Dhindsa RS, Bradrick SS, Yao X, Heinzen EL, Petrovski S, Krueger BJ, Johnson MR, Frankel WN, Petrou S, Boumil RM, and Goldstein DB (2015). Epileptic encephalopathy-causing mutations in DNM1 impair synaptic vesicle endocytosis. Neurol. Genet 1, e4. [PubMed: 27066543]

Diz-Muñoz A, Fletcher DA, and Weiner OD (2013). Use the force: membrane tension as an organizer of cell shape and motility. Trends Cell Biol. 23, 47–53. [PubMed: 23122885]

Doherty GJ, and McMahon HT (2009). Mechanisms of endocytosis. Annu. Rev. Biochem 78, 857–902. [PubMed: 19317650]

Doyon JB, Zeitler B, Cheng J, Cheng AT, Cherone JM, Santiago Y, Lee AH, Vo TD, Doyon Y, Miller JC, et al. (2011). Rapid and efficient clathrin-mediated endocytosis revealed in genome-edited mammalian cells. Nat. Cell Biol 13, 331–337. [PubMed: 21297641]

Francis KR, Ton AN, Xin Y, O'Halloran PE, Wassif CA, Malik N, Williams IM, Cluzeau CV, Trivedi NS, Pavan WJ, et al. (2016). Modeling Smith-Lemli-Opitz syndrome with induced pluripotent stem cells reveals a causal role for Wnt/β-catenin defects in neuronal cholesterol synthesis phenotypes. Nat. Med 22, 388–396. [PubMed: 26998835]

Frey F, and Schwarz US (2020). Competing pathways for the invagination of clathrin-coated membranes. Soft Matter 16, 10723–10733. [PubMed: 33107553]

Futter C, Meschede IP, Wavre ST, Silva MLD, Tolmachova T, and Seabra MC (2012). Phagosome Maturation And Interactions With The Endocytic Pathway In Retinal Pigment Epithelial Cells. Invest. Ophthalmol. Vis. Sci 53, 3701, 3701.

Ge S, White JG, and Haynes CL (2010). Critical role of membrane cholesterol in exocytosis revealed by single platelet study. ACS Chem. Biol 5, 819–828. [PubMed: 20590163]

Gondré-Lewis MC, Petrache HI, Wassif CA, Harries D, Parsegian A, Porter FD, and Loh YP (2006). Abnormal sterols in cholesterol-deficiency diseases cause secretory granule malformation and decreased membrane curvature. J. Cell Sci 119, 1876–1885. [PubMed: 16636072]

Gou-Fàbregas M, Macià A, Anerillas C, Vaquero M, Jové M, Jain S, Ribera J, and Encinas M (2016). 7-dehydrocholesterol efficiently supports Ret signaling in a mouse model of Smith-Opitz-Lemli syndrome. Sci. Rep 6, 28534. [PubMed: 27334845]

Grassart A, Cheng AT, Hong SH, Zhang F, Zenzer N, Feng Y, Briner DM, Davis GD, Malkov D, and Drubin DG (2014). Actin and dynamin2 dynamics and interplay during clathrin-mediated endocytosis. J. Cell Biol 205, 721–735. [PubMed: 24891602]

Hamilton JA (2003). Fast flip-flop of cholesterol and fatty acids in membranes: implications for membrane transport proteins. Curr. Opin. Lipidol 14, 263–271. [PubMed: 12840657]

Hansen GH, Pedersen J, Niels-Christiansen LL, Immerdal L, and Danielsen EM (2003). Deep-apical tubules: dynamic lipid-raft microdomains in the brush-border region of enterocytes. Biochem. J 373, 125–132. [PubMed: 12689332]

Hassinger JE, Oster G, Drubin DG, and Rangamani P (2017). Design principles for robust vesiculation in clathrin-mediated endocytosis. Proc. Natl. Acad. Sci. USA 114, E1118–E1127. [PubMed: 28126722]

Haucke V, and Kozlov MM (2018). Membrane remodeling in clathrin-mediated endocytosis. J. Cell Sci 131, jcs216812. [PubMed: 30177505]

Helfrich W (1973). Elastic properties of lipid bilayers: theory and possible experiments. Z. Naturforsch C 28, 693–703.

Henriksen J, Rowat AC, and Ipsen JH (2004). Vesicle fluctuation analysis of the effects of sterols on membrane bending rigidity. Eur. Biophys. J 33, 732–741. [PubMed: 15221234]

Hilgemann DW, Lin MJ, Fine M, and Deisl C (2020). On the existence of endocytosis driven by membrane phase separations. Biochim. Biophys. Acta Biomembr 1862, 183007. [PubMed: 31202864]

Hirama T, Lu SM, Kay JG, Maekawa M, Kozlov MM, Grinstein S, and Fairn GD (2017). Membrane curvature induced by proximity of anionic phospholipids can initiate endocytosis. Nat. Commun 8, 1393. [PubMed: 29123120]

Honda M, Tint GS, Honda A, Nguyen LB, Chen TS, and Shefer S (1998). 7-Dehydrocholesterol down-regulates cholesterol biosynthesis in cultured Smith-Lemli-Opitz syndrome skin fibroblasts. J. Lipid Res 39, 647–657. [PubMed: 9548596]

Huttner WB, and Zimmerberg J (2001). Implications of lipid microdomains for membrane curvature, budding and fission. Curr. Opin. Cell Biol 13, 478–484. [PubMed: 11454455]

Irons M, Elias ER, Salen G, Tint GS, and Batta AK (1993). Defective cholesterol biosynthesis in Smith-Lemli-Opitz syndrome. Lancet 341, 1414.

Jiang XS, Wassif CA, Backlund PS, Song L, Holtzclaw LA, Li Z, Yergey AL, and Porter FD (2010). Activation of Rho GTPases in Smith-Lemli-Opitz syndrome: pathophysiological and clinical implications. Hum. Mol. Genet 19, 1347–1357. [PubMed: 20067919]

Jülicher F, and Lipowsky R (1993). Domain-induced budding of vesicles. Phys. Rev. Lett 70, 2964–2967. [PubMed: 10053698]

Jülicher F, and Lipowsky R (1996). Shape transformations of vesicles with intramembrane domains. Phys. Rev. E Stat. Phys. Plasmas Fluids Relat. Interdiscip. Topics 53, 2670–2683. [PubMed: 9964554]

Kaksonen M, and Roux A (2018). Mechanisms of clathrin-mediated endocytosis. Nat. Rev. Mol. Cell Biol 19, 313–326. [PubMed: 29410531]

Keller RK, Arnold TP, and Fliesler SJ (2004). Formation of 7-dehydrocholesterol-containing membrane rafts in vitro and in vivo, with relevance to the Smith-Lemli-Opitz syndrome. J. Lipid Res 45, 347–355. [PubMed: 14594996]

Kelley RI (1995). Diagnosis of Smith-Lemli-Opitz syndrome by gas chromatography/mass spectrometry of 7-dehydrocholesterol in plasma, amniotic fluid and cultured skin fibroblasts. Clin. Chim. Acta 236, 45–58. [PubMed: 7664465]

Khatibzadeh N, Gupta S, Farrell B, Brownell WE, and Anvari B (2012). Effects of cholesterol on nano-mechanical properties of the living cell plasma membrane. Soft Matter 8, 8350–8360. [PubMed: 23227105]

Kim JH, Singh A, Del Poeta M, Brown DA, and London E (2017). The effect of sterol structure upon clathrin-mediated and clathrin-independent endocytosis. J. Cell Sci 130, 2682–2695. [PubMed: 28655854]

Kolf-Clauw M, Chevy F, Wolf C, Siliart B, Citadelle D, and Roux C (1996). Inhibition of 7-dehydrocholesterol reductase by the teratogen AY9944: a rat model for Smith-Lemli-Opitz syndrome. Teratology 54, 115–125. [PubMed: 8987154]

Krakowiak PA, Nwokoro NA, Wassif CA, Battaile KP, Nowaczyk MJ, Connor WE, Maslen C, Steiner RD, and Porter FD (2000). Mutation analysis and description of sixteen RSH/Smith-Lemli-Opitz syndrome patients: polymerase chain reaction-based assays to simplify genotyping. Am. J. Med. Genet 94, 214–227. [PubMed: 10995508]

Krishna A, and Sengupta D (2019). Interplay between Membrane Curvature and Cholesterol: Role of Palmitoylated Caveolin-1. Biophys. J 116, 69–78. [PubMed: 30579563]

Kusumi A, Fujiwara TK, Chadda R, Xie M, Tsunoyama TA, Kalay Z, Kasai RS, and Suzuki KG (2012). Dynamic organizing principles of the plasma membrane that regulate signal transduction: commemorating the fortieth anniversary of Singer and Nicolson's fluid-mosaic model. Annu. Rev. Cell Dev. Biol 28, 215–250. [PubMed: 22905956]

Kwik J, Boyle S, Fooksman D, Margolis L, Sheetz MP, and Edidin M (2003). Membrane cholesterol, lateral mobility, and the phosphatidylinositol 4,5-bisphosphate-dependent organization of cell actin. Proc. Natl. Acad. Sci. USA 100, 13964–13969. [PubMed: 14612561]

Lange Y, Dolde J, and Steck TL (1981). The rate of transmembrane movement of cholesterol in the human erythrocyte. J. Biol. Chem 256, 5321–5323. [PubMed: 7240138]

Lange Y, Swaisgood MH, Ramos BV, and Steck TL (1989). Plasma membranes contain half the phospholipid and 90% of the cholesterol and sphingomyelin in cultured human fibroblasts. J. Biol. Chem 264, 3786–3793. [PubMed: 2917977]

Leibler S (1986). Curvature instability in membranes. J. Phys. (Paris) 47, 507–516.

Lentz BR, Siegel DP, and Malinin V (2002). Filling potholes on the path to fusion pores. Biophys. J 82, 555–557. [PubMed: 11806900]

Levental I, Levental KR, and Heberle FA (2020). Lipid Rafts: Controversies Resolved, Mysteries Remain. Trends Cell Biol. 30, 341–353. [PubMed: 32302547]

Linck LM, Lin DS, Flavell D, Connor WE, and Steiner RD (2000). Cholesterol supplementation with egg yolk increases plasma cholesterol and decreases plasma 7-dehydrocholesterol in Smith-Lemli-Opitz syndrome. Am. J. Med. Genet 93, 360–365. [PubMed: 10951458]

Liu J, Sun Y, Drubin DG, and Oster GF (2009). The mechanochemistry of endocytosis. PLoS Biol. 7, e1000204. [PubMed: 19787029]

Lu F, Liang Q, Abi-Mosleh L, Das A, De Brabander JK, Goldstein JL, and Brown MS (2015). Identification of NPC1 as the target of U18666A, an inhibitor of lysosomal cholesterol export and Ebola infection. eLife 4, e12177. [PubMed: 26646182]

Luo J, Jiang LY, Yang H, and Song BL (2019). Intracellular Cholesterol Transport by Sterol Transfer Proteins at Membrane Contact Sites. Trends Biochem. Sci 44, 273–292. [PubMed: 30415968]

Maxfield FR, and Tabas I (2005). Role of cholesterol and lipid organization in disease. Nature 438, 612–621. [PubMed: 16319881]

McMahon HT, and Gallop JL (2005). Membrane curvature and mechanisms of dynamic cell membrane remodelling. Nature 438, 590–596. [PubMed: 16319878]

Megha B, Bakht O, and London E (2006). Cholesterol precursors stabilize ordinary and ceramide-rich ordered lipid domains (lipid rafts) to different degrees. Implications for the Bloch hypothesis and sterol biosynthesis disorders. J. Biol. Chem 281, 21903–21913. [PubMed: 16735517]

Miller SE, Mathiasen S, Bright NA, Pierre F, Kelly BT, Kladt N, Schauss A, Merrifield CJ, Stamou D, Höning S, and Owen DJ (2015). CALM regulates clathrin-coated vesicle size and maturation by directly sensing and driving membrane curvature. Dev. Cell 33, 163–175. [PubMed: 25898166]

Morlot S, Galli V, Klein M, Chiaruttini N, Manzi J, Humbert F, Dinis L, Lenz M, Cappello G, and Roux A (2012). Membrane shape at the edge of the dynamin helix sets location and duration of the fission reaction. Cell 151, 619–629. [PubMed: 23101629]

Murthy VN, and Stevens CF (1998). Synaptic vesicles retain their identity through the endocytic cycle. Nature 392, 497–501. [PubMed: 9548254]

Najafinobar N, Mellander LJ, Kurczy ME, Dunevall J, Angerer TB, Fletcher JS, and Cans A-S (2016). Cholesterol Alters the Dynamics of Release in Protein Independent Cell Models for Exocytosis. Sci. Rep 6, 33702. [PubMed: 27650365]

Narayana YV, Gadgil C, Mote RD, Rajan R, and Subramanyam D (2019). Clathrin-Mediated Endocytosis Regulates a Balance between Opposing Signals to Maintain the Pluripotent State of Embryonic Stem Cells. Stem Cell Reports 12, 152–164. [PubMed: 30554918]

Nohturfft A, Brown MS, and Goldstein JL (1998). Sterols regulate processing of carbohydrate chains of wild-type SREBP cleavage-activating protein (SCAP), but not sterol-resistant mutants Y298C or D443N. Proc. Natl. Acad. Sci. USA 95, 12848–12853. [PubMed: 9789003]

Ory DS, Ottinger EA, Farhat NY, King KA, Jiang X, Weissfeld L, Berry-Kravis E, Davidson CD, Bianconi S, Keener LA, et al. (2017). Intrathecal 2-hydroxypropyl-β-cyclodextrin decreases neurological disease progression in Niemann-Pick disease, type C1: a non-randomised, open-label, phase 1–2 trial. Lancet 390, 1758–1768. [PubMed: 28803710]

Rahier A, and Taton M (1996). Sterol biosynthesis: strong inhibition of maize delta 5,7-sterol delta 7-reductase by novel 6-aza-B-homosteroids and other analogs of a presumptive carbocationic intermediate of the reduction reaction. Biochemistry 35, 7069–7076. [PubMed: 8679532]

Ramachandra Rao S, Pfeffer BA, Más Gómez N, Skelton LA, Keiko U, Sparrow JR, Rowsam AM, Mitchell CH, and Fliesler SJ (2018). Compromised phagosome maturation underlies RPE

pathology in cell culture and whole animal models of Smith-Lemli-Opitz Syndrome. Autophagy 14, 1796–1817. [PubMed: 29979914]

Rodal SK, Skretting G, Garred O, Vilhardt F, van Deurs B, and Sandvig K (1999). Extraction of cholesterol with methyl-beta-cyclodextrin perturbs formation of clathrin-coated endocytic vesicles. Mol. Biol. Cell 10, 961–974. [PubMed: 10198050]

Róg T, Stimson LM, Pasenkiewicz-Gierula M, Vattulainen I, and Karttunen M (2008). Replacing the cholesterol hydroxyl group with the ketone group facilitates sterol flip-flop and promotes membrane fluidity. J. Phys. Chem. B 112, 1946–1952. [PubMed: 18217743]

Rothberg KG, Ying YS, Kamen BA, and Anderson RG (1990). Cholesterol controls the clustering of the glycophospholipid-anchored membrane receptor for 5-methyltetrahydrofolate. J. Cell Biol 111, 2931–2938. [PubMed: 2148564]

Rothberg KG, Heuser JE, Donzell WC, Ying YS, Glenney JR, and Anderson RG (1992). Caveolin, a protein component of caveolae membrane coats. Cell 68, 673–682. [PubMed: 1739974]

Roux A, Uyhazi K, Frost A, and De Camilli P (2006). GTP-dependent twisting of dynamin implicates constriction and tension in membrane fission. Nature 441, 528–531. [PubMed: 16648839]

Saheki Y, and De Camilli P (2012). Synaptic vesicle endocytosis. Cold Spring Harb. Perspect. Biol 4, a005645. [PubMed: 22763746]

Saleem M, Morlot S, Hohendahl A, Manzi J, Lenz M, and Roux A (2015). A balance between membrane elasticity and polymerization energy sets the shape of spherical clathrin coats. Nat. Commun 6, 6249. [PubMed: 25695735]

Schreiber JM, Lanham DC, Trescher WH, Sparks SE, Wassif CA, Caffo BS, Porter FD, Tierney E, Gropman AL, and Ewen JB (2014). Variations in EEG discharges predict ADHD severity within individual Smith-Lemli-Opitz patients. Neurology 83, 151–159. [PubMed: 24920862]

Scott BL, Sochacki KA, Low-Nam ST, Bailey EM, Luu Q, Hor A, Dickey AM, Smith S, Kerkvliet JG, Taraska JW, and Hoppe AD (2018). Membrane bending occurs at all stages of clathrin-coat assembly and defines endocytic dynamics. Nat. Commun 9, 419. [PubMed: 29379015]

Sengupta P, Baird B, and Holowka D (2007). Lipid rafts, fluid/fluid phase separation, and their relevance to plasma membrane structure and function. Semin. Cell Dev. Biol 18, 583–590. [PubMed: 17764993]

Serfis AB, Brancato S, and Fliesler SJ (2001). Comparative behavior of sterols in phosphatidylcholine-sterol monolayer films. Biochim. Biophys. Acta 1511, 341–348. [PubMed: 11286977]

Sikora DM, Ruggiero M, Petit-Kekel K, Merkens LS, Connor WE, and Steiner RD (2004). Cholesterol supplementation does not improve developmental progress in Smith-Lemli-Opitz syndrome. J. Pediatr 144, 783–791. [PubMed: 15192627]

Skruzny M, Brach T, Ciuffa R, Rybina S, Wachsmuth M, and Kaksonen M (2012). Molecular basis for coupling the plasma membrane to the actin cytoskeleton during clathrin-mediated endocytosis. Proc. Natl. Acad. Sci. USA 109, E2533–E2542. [PubMed: 22927393]

Smith DW, Lemli L, and Opitz JM (1964). A newly recognized syndromeof multiple congenital anomalies. J. Pediatr 64, 210–217. [PubMed: 14119520]

Sochacki KA, Shtengel G, van Engelenburg SB, Hess HF, and Taraska JW (2014). Correlative super-resolution fluorescence and metal-replica transmission electron microscopy. Nat. Methods 11, 305–308. [PubMed: 24464288]

Sochacki KA, Dickey AM, Strub MP, and Taraska JW (2017). Endocytic proteins are partitioned at the edge of the clathrin lattice in mammalian cells. Nat. Cell Biol 19, 352–361. [PubMed: 28346440]

Sodt AJ, Venable RM, Lyman E, and Pastor RW (2016). Nonadditive Compositional Curvature Energetics of Lipid Bilayers. Phys. Rev. Lett 117, 138104. [PubMed: 27715135]

Song J, and Waugh RE (1993). Bending rigidity of SOPC membranes containing cholesterol. Biophys. J 64, 1967–1970. [PubMed: 8369417]

Srinivasan S, Burckhardt CJ, Bhave M, Chen Z, Chen PH, Wang X, Danuser G, and Schmid SL (2018). A noncanonical role for dynamin-1 in regulating early stages of clathrin-mediated endocytosis in non-neuronal cells. PLoS Biol. 16, e2005377. [PubMed: 29668686]

Steck TL, Ye J, and Lange Y (2002). Probing red cell membrane cholesterol movement with cyclodextrin. Biophys. J 83, 2118–2125. [PubMed: 12324429]

Subtil A, Gaidarov I, Kobylarz K, Lampson MA, Keen JH, and McGraw TE (1999). Acute cholesterol depletion inhibits clathrin-coated pit budding. Proc. Natl. Acad. Sci. USA 96, 6775–6780. [PubMed: 10359788]

Sun LP, Li L, Goldstein JL, and Brown MS (2005). Insig required for sterol-mediated inhibition of Scap/SREBP binding to COPII proteins in vitro. J. Biol. Chem 280, 26483–26490. [PubMed: 15899885]

Svoboda MD, Christie JM, Eroglu Y, Freeman KA, and Steiner RD (2012). Treatment of Smith-Lemli-Opitz syndrome and other sterol disorders. Am. J. Med. Genet. C. Semin. Med. Genet 160C, 285–294. [PubMed: 23042642]

Taylor MJ, Perrais D, and Merrifield CJ (2011). A high precision survey of the molecular dynamics of mammalian clathrin-mediated endocytosis. PLoS Biol. 9, e1000604. [PubMed: 21445324]

Tint GS, Irons M, Elias ER, Batta AK, Frieden R, Chen TS, and Salen G (1994). Defective cholesterol biosynthesis associated with the Smith-Lemli-Opitz syndrome. N. Engl. J. Med 330, 107–113. [PubMed: 8259166]

Tint GS, Salen G, Batta AK, Shefer S, Irons M, Elias ER, Abuelo DN, Johnson VP, Lambert M, Lutz R, et al. (1995). Correlation of severity and outcome with plasma sterol levels in variants of the Smith-Lemli-Opitz syndrome. J. Pediatr 127, 82–87. [PubMed: 7608816]

Tu C, Li J, Jiang X, Sheflin LG, Pfeffer BA, Behringer M, Fliesler SJ, and Qu J (2013). Ion-current-based proteomic profiling of the retina in a rat model of Smith-Lemli-Opitz syndrome. Mol. Cell. Proteomics 12, 3583–3598. [PubMed: 23979708]

Tulenko TN, Boeze-Battaglia K, Mason RP, Tint GS, Steiner RD, Connor WE, and Labelle EF (2006). A membrane defect in the pathogenesis of the Smith-Lemli-Opitz syndrome. J. Lipid Res 47, 134–143. [PubMed: 16258167]

van Rheenen J, Achame EM, Janssen H, Calafat J, and Jalink K (2005). PIP2 signaling in lipid domains: a critical re-evaluation. EMBO J. 24, 1664–1673. [PubMed: 15861130]

Vecsernyés M, Fenyvesi F, Bácskay I, Deli MA, Szente L, and Fenyvesi É (2014). Cyclodextrins, blood-brain barrier, and treatment of neurological diseases. Arch. Med. Res 45, 711–729. [PubMed: 25482528]

Vedhachalam C, Duong PT, Nickel M, Nguyen D, Dhanasekaran P, Saito H, Rothblat GH, Lund-Katz S, and Phillips MC (2007). Mechanism of ATP-binding cassette transporter A1-mediated cellular lipid efflux to apolipoprotein A-I and formation of high density lipoprotein particles. J. Biol. Chem 282, 25123–25130. [PubMed: 17604270]

Wang N, Kwan C, Gong X, de Chaves EP, Tse A, and Tse FW (2010). Influence of cholesterol on catecholamine release from the fusion pore of large dense core chromaffin granules. J. Neurosci 30, 3904–3911. [PubMed: 20237261]

Wassif CA, Maslen C, Kachilele-Linjewile S, Lin D, Linck LM, Connor WE, Steiner RD, and Porter FD (1998). Mutations in the human sterol delta7-reductase gene at 11q12–13 cause Smith-Lemli-Opitz syndrome. Am. J. Hum. Genet 63, 55–62. [PubMed: 9634533]

Wassif CA, Vied D, Tsokos M, Connor WE, Steiner RD, and Porter FD (2002). Cholesterol storage defect in RSH/Smith-Lemli-Opitz syndrome fibroblasts. Mol. Genet. Metab 75, 325–334. [PubMed: 12051964]

Wassif CA, Krakowiak PA, Wright BS, Gewandter JS, Sterner AL, Javitt N, Yergey AL, and Porter FD (2005). Residual cholesterol synthesis and simvastatin induction of cholesterol synthesis in Smith-Lemli-Opitz syndrome fibroblasts. Mol. Genet. Metab 85, 96–107. [PubMed: 15896653]

Wassif CA, Kratz L, Sparks SE, Wheeler C, Bianconi S, Gropman A, Calis KA, Kelley RI, Tierney E, and Porter FD (2017). A placebo-controlled trial of simvastatin therapy in Smith-Lemli-Opitz syndrome. Genet. Med 19, 297–305. [PubMed: 27513191]

Watanabe S, Trimbuch T, Camacho-Pérez M, Rost BR, Brokowski B, Söhl-Kielczynski B, Felies A, Davis MW, Rosenmund C, and Jorgensen EM (2014). Clathrin regenerates synaptic vesicles from endosomes. Nature 515, 228–233. [PubMed: 25296249]

Waterham HR, and Hennekam RC (2012). Mutational spectrum of Smith-Lemli-Opitz syndrome. Am. J. Med. Genet. C. Semin. Med. Genet 160C, 263–284. [PubMed: 23042628]

Wenz JJ, and Barrantes FJ (2003). Steroid structural requirements for stabilizing or disrupting lipid domains. Biochemistry 42, 14267–14276. [PubMed: 14640695]

Winterstein C, Trotter J, and Krämer-Albers E-M (2008). Distinct endocytic recycling of myelin proteins promotes oligodendroglial membrane remodeling. J. Cell Sci 121, 834–842. [PubMed: 18303048]

Yue HY, and Xu J (2015). Cholesterol regulates multiple forms of vesicle endocytosis at a mammalian central synapse. J. Neurochem 134, 247–260. [PubMed: 25893258]

Highlights

- Sterol homeostasis regulates membrane bending dynamics and ultrastructure during CME
- Multiple CME steps, including pit formation and scission, are regulated by sterols
- Productive CME requires the presence of sterols with specific biophysical properties
- CME deficits are present within Smith-Lemli-Opitz syndrome patient cell lines

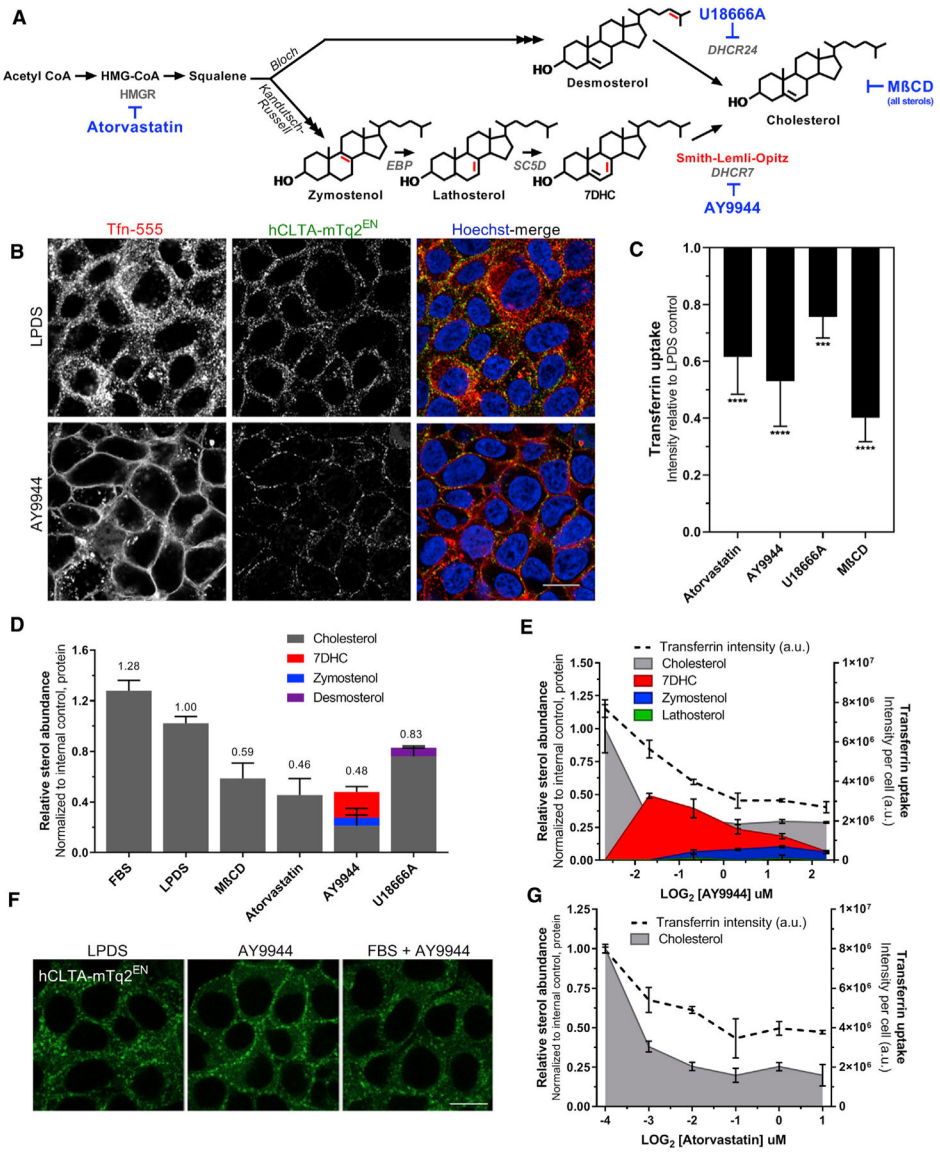

Figure 1. Sterol homeostasis is required for endogenous clathrin trafficking

(A) Schematic illustrating the final steps of post-squalene cholesterol synthesis. Structural alterations of sterol precursors relative to cholesterol are indicated in red. Small molecules used in this study are noted in blue.

(B) Sterol profiles of HEK293T hCLTA^{EN}-mTq2 cells cultured in cholesterol-replete FBS or 7.5% delipidated (LPDS) serum ± various treatments (mean ± SD).

(C) FBS prevents AY9944-mediated CME trafficking defects. Scale bar, 10 μm.

(D) Transferrin (Tfn) uptake under sterol-depleted conditions (mean ± SD). One-way ANOVA ($F(4,40) = 38.57$, $p < 0.0001$) and Dunnett's test versus LPDS control ($n = 9$ biological replicates from 3 independent experiments, 2,000–4,000 cells per replicate).

(E) Sterol depletion results in the accumulation of clathrin at the cell periphery and functional impairment of Tfn internalization in HEK293T hCLTA^{EN}-mTq2 cells. Scale bar, 10 μm.

(F and G) Tfn uptake correlates with sterol content by GC-MS analysis (mean ± SD). n = 3 biological replicates for Tfn uptake and n = 2 biological replicates for sterol analysis performed in parallel.

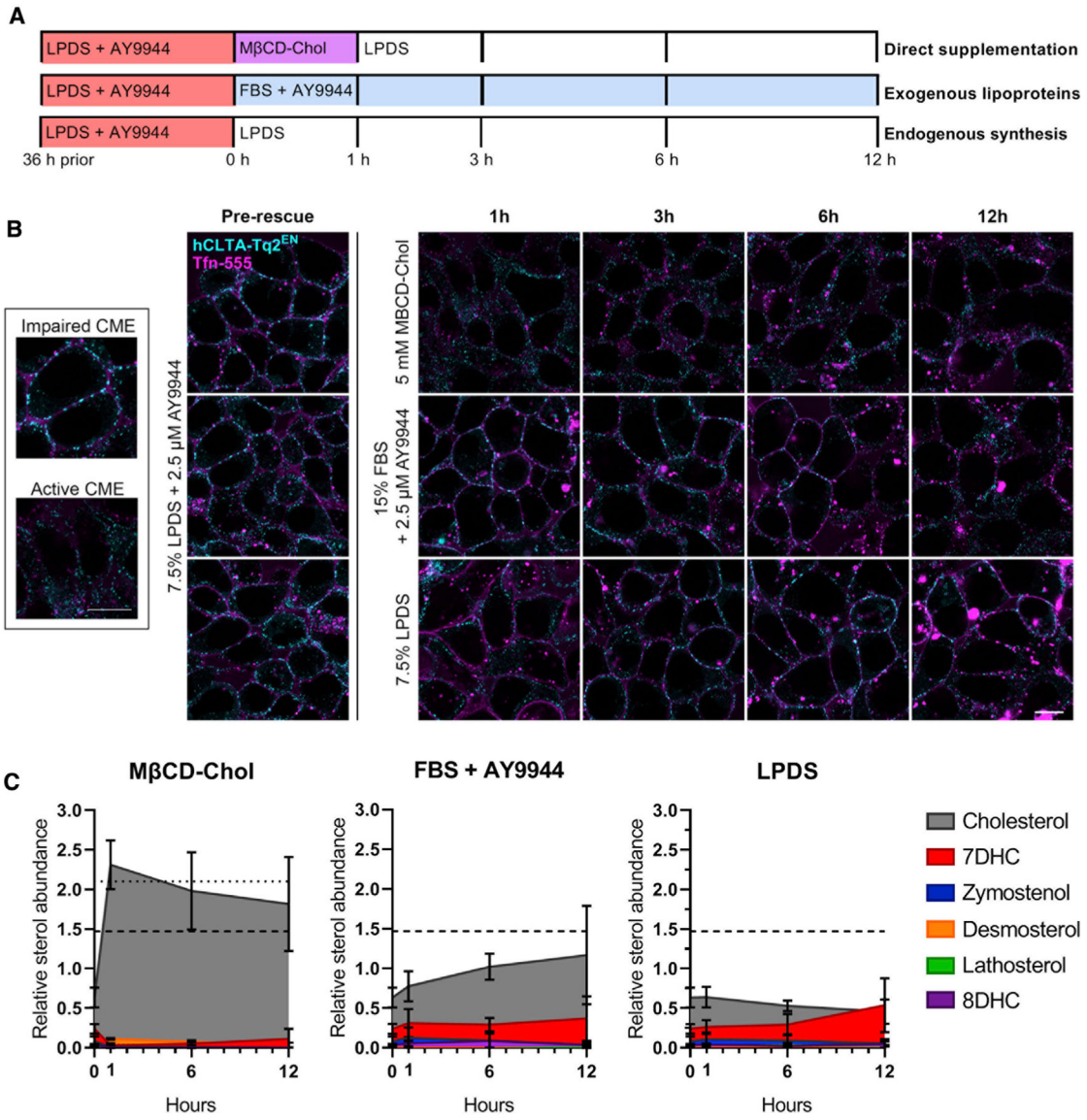

Figure 2. AY9944-induced clathrin trafficking deficits are rescued by direct cholesterol loading

(A) Overview of recovery conditions following AY9944 sterol depletion, including MβCD-Chol and LPDS media chase (top), culture in lipoprotein-rich 15% FBS in the presence of AY9944 (middle), or culture in 7.5% LPDS in the absence of AY9944 to allow endogenous cholesterol synthesis (bottom).

(B) Mid-plane live-cell confocal microscopy of HEK293T hCLTA-Tq2^{EN} following addition of Tfn-conjugated to AF-555 (Tfn-555) during recovery as described in (A). Representative images shown. Tfn and clathrin distribution in normal and arrested CME (inset). Scale bar, 10 μm.

(C) Cellular sterol profiles quantified by GC-MS (mean ± SD). n = 3 biological replicates from independent experiments. Dotted and dashed lines represent total sterol abundance of untreated FBS and LPDS cultures, respectively.

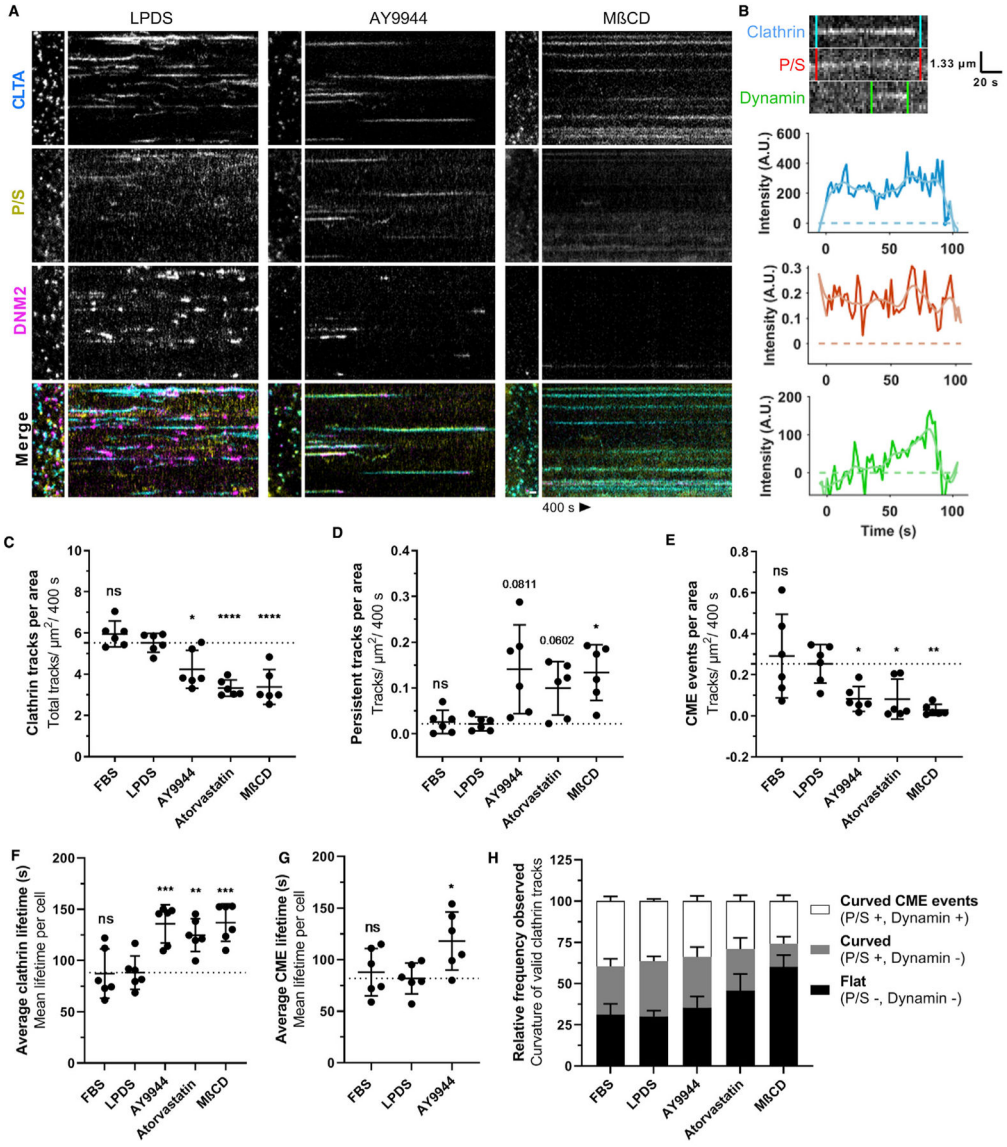

Figure 3. Loss of cholesterol homeostasis disrupts clathrin-coated pit dynamics

(A) Representative polTIRFM kymographs comparing SK-MEL-2 (hCLTA-mTq2^{EN}/ hDNM2-eGFP^{EN}) cells grown in 10% LPDS (left) to moderate sterol depletion with AY9944 (middle) or severe sterol depletion with MβCD (right). Positive curvature generation is indicated by the ratio of P/S fluorescence in DiI-labeled membrane. Time, 400 s. Scale bar, 1 µm.

(B) Representative kymograph of CLTA-mTq2, membrane bending (P/S), and DNM2-eGFP and corresponding intensity traces during a CME event.

(C) Unique clathrin events tracked per cell area (mean ± SD). One-way ANOVA ($F(4,25) = 18.86$, $p < 0.0001$) and Dunnett's test versus LPDS control (n = 6 cells from 2–4 independent experiments, 3,000–30,000 tracks analyzed per cell).

(D) Number of persistent tracks (lifetime, >400 s) per cell area analyzed (mean ± SD). Adjusted p values; *p < 0.05; Welch ANOVA ($F(4, 11.43) = 7.531$, $p = 0.0032$) and Dunnett's T3 test versus LPDS control (n = 6 cells from 2–4 independent experiments).
(E) Productive CME events per cell area (mean ± SD). Welch ANOVA ($F(4,11.24) = 8.948$, $p = 0.0017$) and Dunnett's T3 test versus LPDS control (n = 6 cells from 2–4 independent experiments).
(F) Average clathrin lifetimes per cell across the indicated treatment groups (mean ± SD). One-way ANOVA ($F(4,25) = 10.46$, $p < 0.0001$) and Dunnett's test versus LPDS control (n = 6 cells from 2–4 independent experiments).
(G) Average lifetime of observable CME events, indicated by concurrent dynamin recruitment per cell, across the indicated groups (mean ± SD). Lifetime of CME limited to observed events of >400 s, such that true lifetimes exceed the estimates presented (400 s). One-way ANOVA ($F(4,15) = 4.408$, $p < 0.0312$) and Dunnett's test versus LPDS control (n = 6 cells from 2–4 independent experiments).
(H) Relative frequency of clathrin tracks observed associated with curvature generation (mean ± SEM, n = 6 cells).

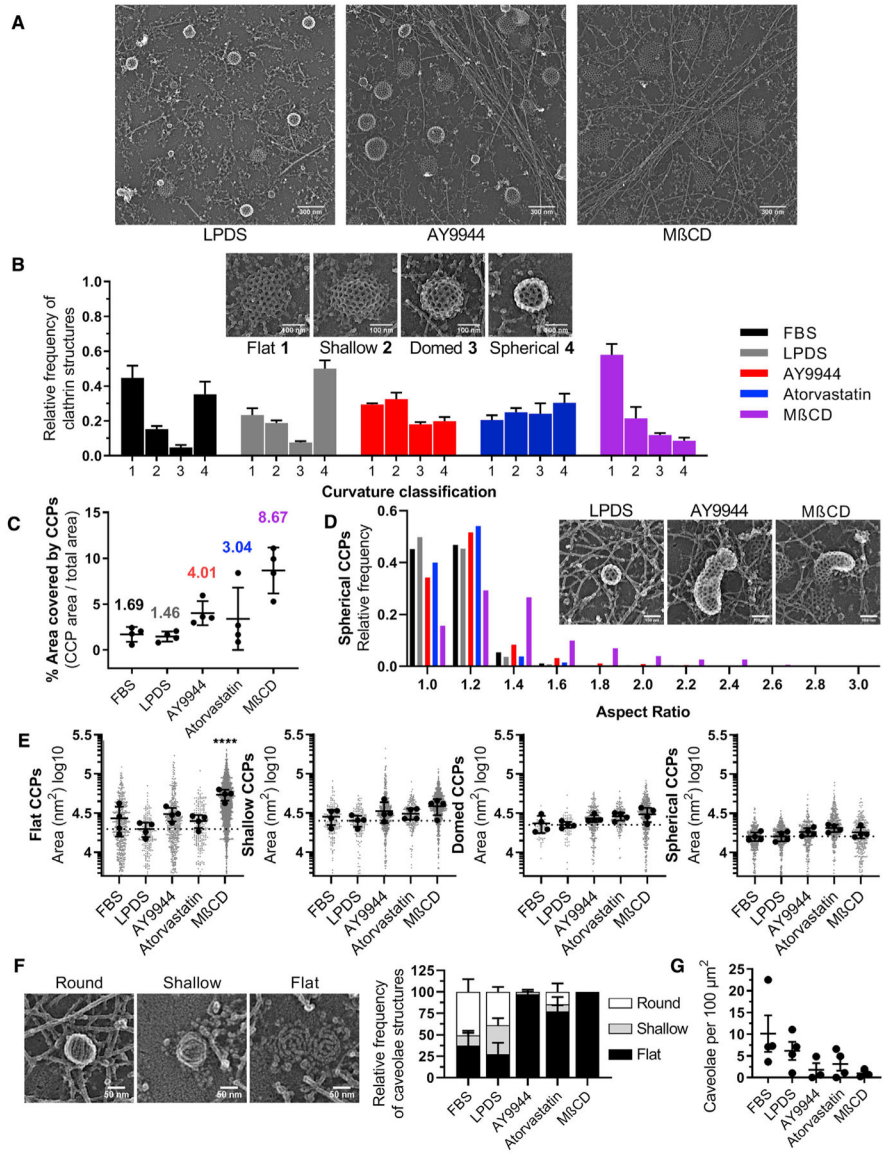

Figure 4. Aberrant clathrin-coated pit ultrastructure under conditions of sterol depletion

(A) Representative platinum-replica transmission electron microscopy (TEM) images from LPDS, AY9944-treated, and MβCD-treated cells.

(B) Relative frequency of clathrin structures by curvature classification (mean ± SEM).

(C) Area of unroofed cells covered by clathrin structures (mean ± SD).

(D) Histogram of spherical clathrin structures showing the distribution of coated pit asymmetry by aspect ratio (major/minor width).

(E) Average area of clathrin-coated structures by curvature classification relative to LPDS controls (mean ± SD). One-way ANOVA ($F(4,15) = 12.91$, $p < 0.0001$) and Dunnett's test versus LPDS control. n = 4 replicas per condition from 2 independent experiments. Total number of clathrin structures analyzed are as follows: FBS = 1164; LPDS = 988; AY9944 = 1700; atorvastatin = 1003; MβCD = 3818.

(F) Representative platinum-replica TEM images of caveolae ultrastructure and relative frequency of structures by curvature classification (mean ± SEM).
(G) Total number of caveolae structures on the membrane per area (mean ± SEM). n = 3–4 replicas per condition from 2 independent experiments. Total number of caveolae structures analyzed are as follows: FBS = 171; LPDS = 89; AY9944 = 21; atorvastatin = 31; MβCD = 13.

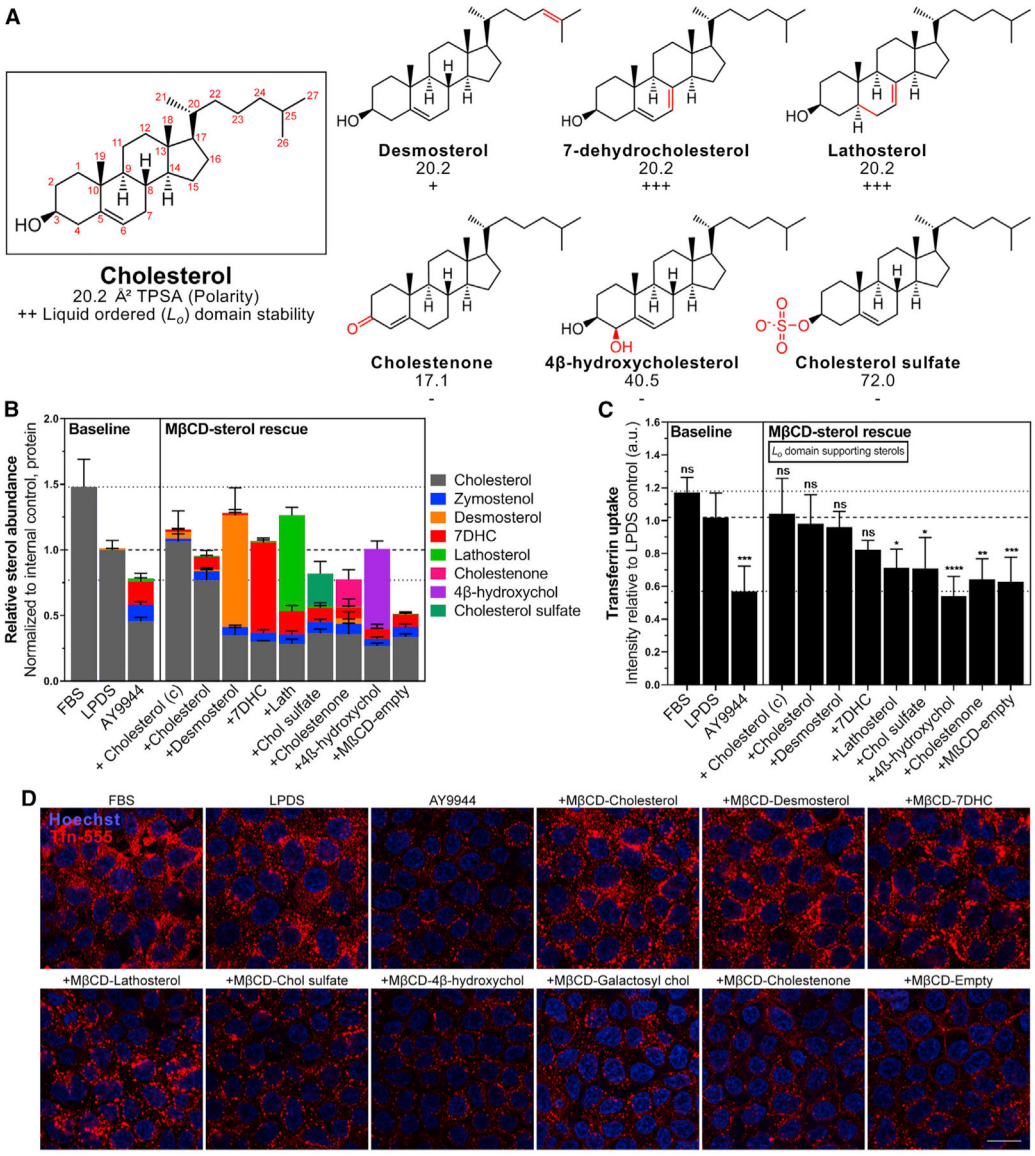

Figure 5. Sterol-mediated phase separation is required to support CME

(A) Summary of physical properties and phase separation behavior of selected sterols. Topological Polar Surface Area (TPSA) computed surface sum over all polar atoms. Ordered lipid (L_o) domain (raft) stabilizing (+) or disrupting (−) sterols are indicated relative to cholesterol (++). Refer to Table S2 for additional details.

(B) Sterol profiles of AY9944-treated HEK293T cells after sterol loading (mean ± SD). n = 4 independent biological replicates from 2 MβCD-sterol preparations.

(C) Tfn uptake relative to LPDS controls (mean ± SD). One-way ANOVA ($F(12, 51) = 11.23$, $p < 0.0001$) and Dunnett's test versus LPDS control (n = 5 biological replicates from 3 independent experiments, ~1,500 cells per replicate). (c), commercially available MβCD-Chol.

(D) Representative mid-plane confocal images after incubation with AF-555 conjugated Tfn. Scale bar, 20 μm.

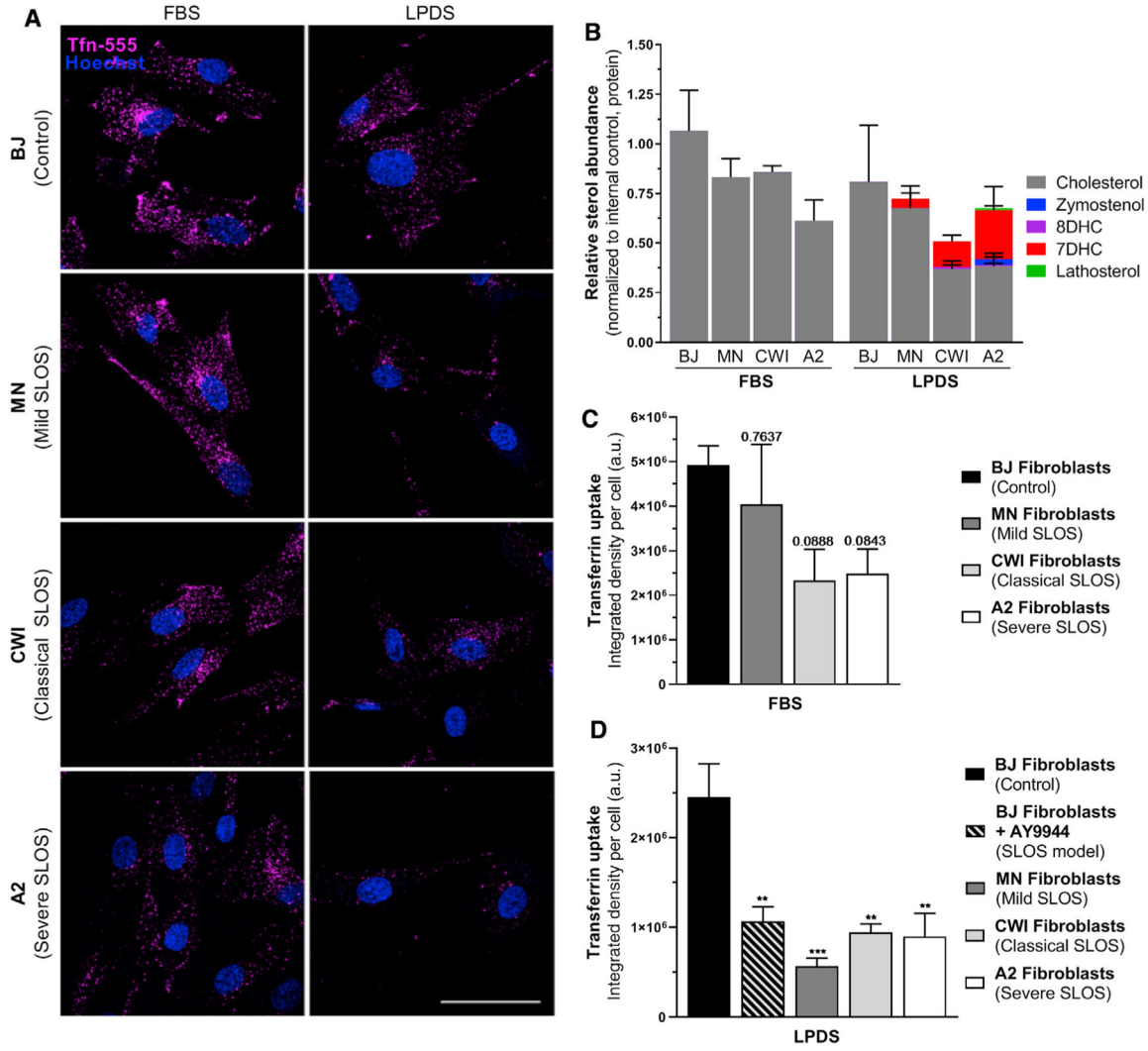

Figure 6. CME dynamics are inhibited within Smith-Lemli-Opitz-syndrome-patient-derived fibroblasts

(A) Representative images of AF-555-conjugated Tfn uptake in control and SLOS fibroblasts grown in FBS or LPDS. Scale bar, 50 μm.

(B) Validation of fibroblast biochemistry by GC-MS.

(C) Tfn uptake in FBS relative to unaffected BJ fibroblasts (mean ± SEM). Adjusted p values, one-way ANOVA ($F(3,10) = 2.916$, $p = 0.0869$) and Dunnett's test versus BJ control ($n = 3–4$ independent replicates, 25 cells per replicate).

(D) Tfn uptake in LPDS relative to unaffected BJ fibroblasts (Mean ± SEM). One-way ANOVA ($F(4,13) = 9.464$, $p = 0.0008$) and Dunnett's test versus BJ control ($n = 2–4$ independent replicates, 25 cells per replicate).

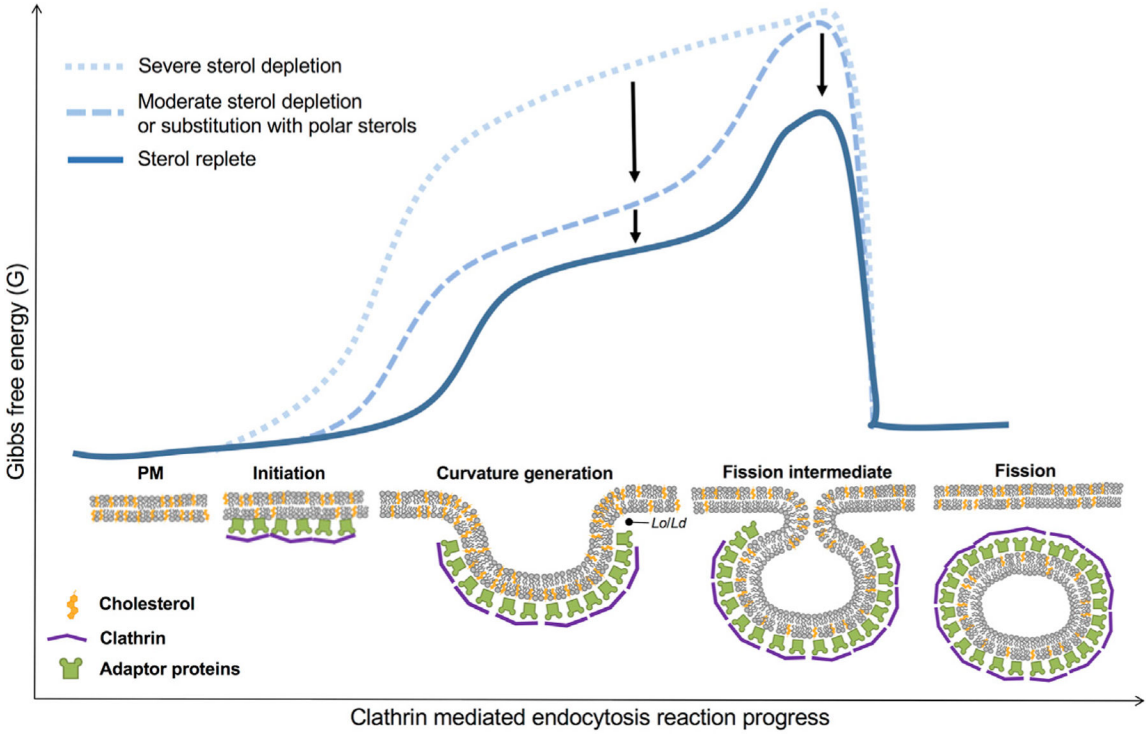

Figure 7. Energy landscape of sterol-mediated membrane bending during clathrin-mediated endocytosis

Cholesterol abundance and sterol identity strongly influence the energetics of membrane bending at multiple stages of clathrin-coated vesicle formation, facilitating curvature initiation and formation of the highly curved vesicle neck. Proposed mechanisms of sterol dynamics during membrane remodeling include cholesterol interleaflet flip-flop, which may relieve compression and expansion of the PM leaflets to negate energy costs associated with PM deformation and tight lipid packing of sterols, which are thought to underlie the formation of L_o and L_d domains (e.g., lipid rafts) to support membrane budding, as increasing curvature minimizes line tension between phase boundaries. The multifaceted properties of sterols likely reduce the energetic requirements necessary for membrane remodeling during clathrin-mediated endocytosis.

KEY RESOURCES TABLE

REAGENT or RESOURCE	SOURCE	IDENTIFIER
Biological samples		
Smith-Lemli-Opitz patient-derived fibroblasts	Gift from Dr. Forbes Porter, NICHD	Refer to Table S3
BJ human fibroblasts, foreskin derived	ATCC	CRL-2522
Chemicals, peptides, and recombinant proteins		
AY9944	Cayman Chemical	Item No. 14611
U-18666A	Cayman Chemical	Item No. 10009085
Atorvastatin	Cayman Chemical	Item No. 10493
Simvastatin	Cayman Chemical	Item No. 10010344
methyl-β-cyclodextrin (MβCD)-cholesterol complex	Sigma	C4951
Alfa Aesar MβCD (1303.31 738 g/mol)	Sigma Aldrich	AAJ6684714
desmosterol	Avanti Polar Lipids	700060
lathosterol	Avanti Polar Lipids	700069
cholestenone	Avanti Polar Lipids	700065
cholesterol sulfate	Avanti Polar Lipids	700016
4β-hydroxycholesterol	Avanti Polar Lipids	700036
7-dehydrocholesterol (7DHC)	Avanti Polar Lipids	70066
cholesterol (ovine)	Avanti Polar Lipids	700000
coprostan-3-ol	Sigma Aldrich	C7578
pyridine (CHROMASOLV Plus for HPLC)	Fischer Scientific	Cat#60-045-737
latrunculin B	Calbiochem	Cat#428020
N,O-bis(trimethylsilyl) trifluoroacetamide with 1% trimethylchlorosilane (BSTFA+ 1% TMCS)	Thermo Fisher	TS-38831
Alexa Fluor™ 555 conjugated Transferrin	Thermo Fisher	T35352
Electron Microscopy Sciences paraformaldehyde	Fisher Scientific	Cat#50-980-494
glutaraldehyde, 8% aqueous solution (EM grade)	Electron Microscopy Sciences	16020
Corning human fibronectin	Fisher Scientific	Cat#CB-40008
Critical commercial assays		
CalPhos™ Mammalian Transfection kit	Clontech	Cat#631312
Pierce MicroBCA Protein Assay	Thermo Scientific	Cat#23235
1,1'-Dioctadecyl-3,3,3′,3′-teramethylindocarboncyanine perchlorate (Dil)	Millipore Sigma	Cat#42364
Experimental models: Cell lines		
Human: HEK293T	ATCC	ACS-4500
Human: HEK293T hCLTA^{EN}-Tq2	This paper	N/A
Human: SK-MEL-2	ATCC	HTB-68
Human: SK-MEL-2 hCLTA^{EN}-Tq2 hDNM2^{EN}-eGFP	Scott et al., 2018	N/A
Oligonucleotides		
CLTA gRNA: 5′-GCAGATGTAGTGTTTCCACA-3′	Eurofins MWG	N/A
Recombinant DNA		

REAGENT or RESOURCE	SOURCE	IDENTIFIER
Cas9 expression vector pX330-U6-Chimeric_BB-CBh-hSpCas9	Cong et al., 2013	Addgene plasmid #42230
pDONOR2 hCLTA-Turquoise2-P2A-PuroR	Anderson et al., 2018	N/A
Software and algorithms		
GraphPad Prism 8.0.2	https://www.graphpad.com/	RRID:SCR_002798
HCS Studio Cell Analysis software	https://www.thermofisher.com/us/en/home/life-science/cell-analysis/cellular-imaging/hcs-hca.html	RRID:SCR_016787
NIS-Elements analysis software	https://www.microscope.healthcare.nikon.com/products/software	RRID:SCR_014329
ImageJ software (v1.8.0)	https://imagej.net/	RRID:SCR_003070
MassHunter (B.08.00)	https://www.agilent.com/en/product/software-informatics	RRID:SCR_015040
MATLAB (2018a)	https://www.mathworks.com/	RRID:SCR_001622
MATLAB script: original CME analysis (cmeAnalysissoftware)	Aguet et al., 2013	https://www.utsouthwestern.edu/labs/danuser/software/; https://github.com/DanuserLab/cmeAnalysis
Other		
FACSJazz™ Cell Sorter	BD Biosciences	https://www.bdbiosciences.com/en-us/products/instruments/flow-cytometers/research-cell-sorters/bd-facsjazz
7890A gas chromatography	Agilent Technologies	https://www.agilent.com/en/product/gas-chromatography
5977B mass spectrometer	Agilent Technologies	https://www.agilent.com/en/product/gas-chromatography-massspectrometry-gc-ms
GC column: 0.18 mm ID × 20 m 1,4-bis(dimethylsiloxy)phenylene dimethyl polysiloxane	Restek	Cat#43602
GC liners: 4 mm ID × 78.5 mm quartz wool liner	Restek	Cat#23309
FluoroDish™ culture plates	World Precision Instruments Inc.	FD35–100
Faramount Mounting Medium Dako	Aglient	3307894